A global 5km monthly potential evapotranspiration dataset (1982–2015) estimated by the Shuttleworth-Wallace model

Shanlei Sun[1], Zaoyin Bi[1], Jingfeng Xiao[2], Yi Liu[3], Ge Sun[4], Weimin Ju[5], Chunwei Liu[6], Mengyuan Mu[7], Jinjian Li[8], Yang Zhou[1], Xiaoyuan Li[1], Yibo Liu[6], Haishan Chen[1]

[1]Collaborative Innovation Center on Forecast and Evaluation of Meteorological Disasters/Key Laboratory of Meteorological Disaster, Ministry of Education/International Joint Research Laboratory on Climate and Environment Change, Nanjing University of Information Science and Technology, Nanjing, China

[2]Earth Systems Research Center, Institute for the Study of Earth, Oceans, and Space, University of New Hampshire, Durham, USA

[3]School of Civil and Environmental Engineering, University of New South Wales, Sydney, Australia

[4]Eastern Forest Environmental Threat Assessment Center, Southern Research Station, USDA Forest Service, Raleigh, USA

[5]International Institute for Earth System Science, Nanjing University, Nanjing, China

[6]Jiangsu Key Laboratory of Agricultural Meteorology, School of Applied Meteorology, Nanjing University of Information Science and Technology, Nanjing, China

[7]ARC Centre of Excellence for Climate Extremes and Climate Change Research Centre, University of New South Wales, Sydney, Australia

[8]School of Atmospheric Sciences/Plateau Atmosphere and Environment Key Laboratory of Sichuan Province, Chengdu University of Information Technology, Chengdu, China

Correspondence to: Shanlei Sun (sun.s@nuist.edu.cn)

Abstract. As the theoretical upper bound of evapotranspiration (ET) or water use by ecosystems, potential ET (PET) has always been widely used as a variable linking a variety of disciplines, such as climatology, ecology, hydrology, and agronomy. However, substantial uncertainties exist in the current PET methods (e.g., empiric models and single-layer models) and datasets, because of unrealistic configurations of land surface and unreasonable parameterizations. Therefore, this study comprehensively considered interspecific differences in various vegetation-related parameters (e.g., plant stomatal resistance and CO_2 effects on stomatal resistance) to calibrate and parametrize the Shuttleworth-Wallace (SW) model for forests, shrubland, grassland and cropland. We derived the parameters using identified daily ET observations with no water stress (i.e., PET) at 96 eddy covariance (EC) sites across the globe. Model validations suggest that the calibrated model could be transferable from known observations to any location. Based on four popular meteorological datasets, relatively realistic canopy height and time-varying land use/land cover and Leaf Area Index, we generated a global 5 km ensemble mean monthly PET dataset that includes two components of potential transpiration (PT) and soil evaporation (PE) for the 1982–2015 time period. Using this new dataset, the climatological characteristics of PET partitioning and the spatio-temporal changes in PET, PE and PT were investigated. The global mean annual PET was 1200 mm with PT/PET of 40% and PE/PET of 60%, and moreover controlled by PT and PE over 43% and 57% of the globe, respectively. Globally, the annual PET and PT significantly ($p<0.05$) increases by 1.25 mm/yr and 1.22 mm/yr over the last 34 years, followed by a slight increase in the annual PE. Overall, the annual PET changes over 53% of the

globe could be attributed to PT, and the rest to PE. The new PET dataset may be used by academic communities and various agencies to conduct climatological analyses, hydrological modelling, drought studies, agricultural water management, and biodiversity conservation. The dataset is available at https://doi.org/10.11888/Terre.tpdc.300193 (Sun et al., 2023).

40   **1 Introduction**

Potential evapotranspiration (PET) is the maximum amount of water that can be transferred to the air from a given land cover (e.g., land and water), providing an upper limit of the evaporative losses from this land cover (Allen et al., 1998; Milly and Dunne, 2016; Xiang et al., 2020). Commonly, it consists of potential evaporation from soils (PE) and/or transpiration by plants (PT) when the soil water supply for evapotranspiration (ET) process is non-limiting (Thornthwaite, 1948; Xiang et al., 2020).

45   The spatio-temporal differences of PET mainly depend on those of climatic conditions, including net radiation, wind speed, the atmospheric vapour deficit, and thus PET is usually regarded as an accepted proxy for the atmospheric evaporative demand. Additionally, PET has been widely used to estimate actual ET (Sun et al., 2011a; Rao et al., 2011; Liu et al., 2017), a critical variable that links water, energy, and carbon cycles (Sun et al., 2011b), and thus is a key variable for a variety of disciplines, such as climatology, ecology, hydrology and agronomy (Allen et al., 1998; Espadafor et al., 2011; Beven, 2012).

50   Historically, numerous PET models have been proposed (Singh and Xu, 1997; Xu and Singh, 2000, 2001; Xiang et al., 2020). In general, the PET models can be grouped into four types: mass-transfer-based ones (e.g., Dalton-type models; Singh and Xu, 1997), which are based on Dalton's law and take observed wind speed and water vapour pressure as inputs; temperature-based ones (e.g., Thornthwaite equation; Thornthwaite, 1948), which take temperature as a proxy for the radiative energy available, along with extraterrestrial radiation estimated from the date of the year and latitude; radiation-based ones (e.g., Turc and

55   Hargreaves models; Turc, 1961; Hargreaves and Samani, 1983), which use measured data such as net solar radiation, sunshine hours or cloudiness factors; and combination ones (e.g., Penman-Monteith models, including its original type and variants; Penman, 1948; Monteith, 1965; Allen et al., 1998), which combine the energy balance with the mass transfer method. Despite low requirement of climatic variables for the former three types of the PET model, they are lack of comprehensive physical considerations of ET process and heavily rely on empirical factors which are dependent on historical or present-day climate

60   for calibration (Tabari and Talaee, 2011; Aschonitis et al., 2015; Tanguy et al., 2018; Xiang et al., 2020). By contrast, the combination models (e.g., Penman-Monteith models) involve relatively comprehensive physical basis, and thus have been widely used by various scientific communities (McVicar et al., 2007; Mu et al., 2013; Sun et al., 2017, 2022). As one of the most famous Penman-Monteith model variant, the Food and Agriculture Organization of the United Nations (FAO)-56 Penman-Monteith model has been validated against lysimeter data across the globe, obtaining reliable results (Jensen et al.,

65   1990; Itenfisu et al., 2000; Berengena and Gavilán, 2005; Trajkovic, 2007; Liu et al., 2017; Gong et al., 2017), and

recommended as a standard tool for calculating PET with climatic data by the International Commission on Irrigation and Drainage (ICID), the FAO and the American Society of Civil Engineers (ASCE).

Despite the relatively satisfactory performance, the Penman-Monteith models still have inherent shortages for parameterization scheme of land surface. For example, these models set the evaporating and/or transpiration surfaces as a whole (i.e., a so-called

70 "big-leaf"), regardless of differences in processes of soil evaporation and plant transpiration (Stannard, 1993; Yang and Shang et al., 2012; Liu et al., 2015). Over a large region, however, the big leaf assumption is rarely valid. Usually, many vegetation types co-exist over the land, and there are always some parts or periods where or when the vegetation not "closed". Some studies have pointed out that such assumption limits the applicability of the Penman-Monteith models under various vegetation distribution conditions, e.g., better (worse) performance under complete and heterogeneous (sparse and inhomogeneous)

75 vegetation distribution conditions (Shuttleworth and Wallace, 1985; Stannard, 1993; Yang and Shang, 2012; Huang et al., 2020). Comprehensively considering differences in processes of soil evaporation and plant transpiration, Shuttleworth and Wallace (1985) extended the Penman-Monteith single-layer models to two-layer model [i.e., Shuttleworth-Wallace (SW) model]. This model divided ET into plant and soil components based on surface resistances to regulate the heat and mass transfer from plant and soil surfaces, as well as aerodynamic resistance to regulate fluxes to the atmosphere (Lagos et al., 2013;

80 Liu et al., 2015; Zhao et al., 2015; Huang et al., 2020). Relative to the Penman-Monteith models, the SW model is the first analytical model combining transpiration and soil evaporation by formulating the different media via which evaporative flux travels as resistances (Kool et al., 2014). This partitioning is crucial for reasonably describing and understanding ET processes (Zhou et al., 2016, 2018). The SW model is generally considered to be more accurate and more physically-based, and has been extensively used at point and regional scales (Brisson et al., 1998; Hu et al., 2009; Kool et al., 2014; Liu et al., 2015; Huang

85 et al., 2020).

It should be noted that there are two major difficulties to run the SW model. Firstly, it has high requirement for meteorological data inputs, including the maximum and minimum air temperatures, relative humidity, wind speed and solar radiation or their proxy data. Commonly, the maximum and minimum air temperatures are measured at meteorological sites, while observations of the other elements are scare, especially when long time series and large spatial coverage are required for climate studies.

90 This may be a major reason that some temperature-based and radiation-based PET models (e.g., Priestley-Taylor and Hargreaves-Samani models) are still widely-used at present, especially for regions with sparse meteorological observations (Aschonitis et al., 2017; Tanguy et al., 2018). Secondly, the SW model is hard to parameterize given the large number of parameters (Brisson et al., 1998; Odhiambo and Irmak, 2011; Kool et al., 2014), and therefore this model is often applied at point and regional scales (Iritz et al., 1999; Yang and Shang, 2012; Liu et al., 2015; Huang et al., 2020; Chen et al., 2022).

95 Fortunately, with the development of observation and numerical simulation technology during the past decades, various global datasets have become available, including meteorological datasets (e.g., Harris et al., 2020; Molod et al., 2015; Hersbach et

al., 2020; Beck et al., 2022), vegetation height (e.g., Simard et al., 2011; Wang et al., 2016; Potapov et al., 2020; Lang et al., 2021, 2022), land use/land cover (LULC) datasets (e.g., Liu et al., 2020), Leaf Area Index (LAI; e.g., Friedl et al., 2010; Liu et al., 2012; Zhu et al., 2013; Xiao et al., 2014), and eddy covariance (EC) flux observations across various ecosystems (e.g.,

100   LaThuile, https://fluxnet.org/data/la-thuile-dataset/; FLUXNET2015, http://fluxnet.fluxdata.org/data/fluxnet2015-dataset/; OzFlux, https://data.ozflux.org.au/portal/home.jspx; and AsiaFlux, http://asiaflux.net/?page_id=23). These released datasets provide a valuable opportunity for parameterizing and driving the SW model at the global scale.

Previous studies have suggested that land surface properties could play a dominant role in controlling variations of the ET process (Sun et al., 2021, 2022). Of the land surface properties, vegetation is the most ever-changing due to plant growth,

105   natural disturbances and anthropogenic disturbances (Liu et al., 2016a, 2016b; Papagiannopoulou et al., 2017; Cavalcante et al., 2019; Zhang et al., 2020). Recently, with climate change and/or intensified human activities, vegetation has greatly changed on regional and even the global scales (Zhu et al., 2016; Chen et al., 2019), including shifts in vegetation types and vegetation greening (i.e., increases in LAI or other vegetation indices), which have altered the allocation of available water and energy (Zhou et al., 2016, 2018; Sun et al., 2022). As an important biophysical parameter of vegetation, the plant stomatal resistance

110   has been widely evidenced to increase with the elevated atmospheric CO_2 concentration by numerous observations and numerical simulations, but the increasing magnitudes differed among vegetation types (Wand et al., 1999; Medlyn et al., 2001; Norby et al., 2005; Franks and Beerling, 2008; Lin et al., 2015; Gardner et al., 2022). The increased plant stomatal resistance could in turn reduce plant transpiration and thereby change the water cycle on regional and even global scales (Gedney et al., 2006; Piao et al., 2007; Sun et al., 2014; Zhao and Cao, 2022; Zhan et al., 2022). Especially, such impacts of elevated CO_2-

115   induced plant stomatal resistance increase on hydrological processes have been proved to be of significance, especially for the future climate change scenarios with the high CO_2 emission (Roderick et al., 2015; Milly and Dunne, 2016; Scheff, 2018; Yang et al., 2019). These suggested that the temporal changes in vegetation (i.e., vegetation types, LAI and plant stomatal resistance) should be involved into the models for accurate PET estimates. However, it is unfortunate that the various existing PET products, such as Climatic Research Unit (CRU) Time-Series (TS) 4.06 (CRU TS4.06; Harris et al., 2020), MOD16 (Running

120   et al., 2017), Global Land Evaporation Amsterdam Model (GLEAM) v3.6 (Miralles et al., 2011; Marten et al., 2017), Priestly-Taylor Jet Propulsion Laboratory (PT-JPL) Model (Fisher et al., 2011) and hPET (Singer et al., 2021), did not fully considered impacts of such vegetation changes on PET, potentially resulting in biases of the estimates from the truth values and then introducing uncertainties into the studies based on these products. As a result, to produce a new PET dataset based on more reasonable parameterizations and more realistic configurations of land surface, is needed.

125   Through making use of various existing datasets, this study comprehensively considered spatio-temporal differences in land surfaces and elevated CO_2-induced biophysical effects on plant stomatal resistance to parameterize the SW model, and produced a new global monthly PET dataset. Specifically, our objectives are: (1) to calibrate the SW model with the EC flux

observations to obtain key parameters for each LULC type, and to evaluate the performance of the calibrated model, (2) to generate a global monthly PET product (including PE and PT) from 1982 to 2015 with the calibrated SW model and various

130   inputs, and (3) to investigate the climatological characteristics of PET partitioning and the spatio-temporal changes in PET and its two components across the globe during 1982–2015.

2. Material and methods

2.1 Data sources

2.1.1 Eddy-covariance measurements

135   For fully utilizing the existing EC measurements, this study collected the half-hourly or hourly FLUXNET2015 Tier-2 (http://fluxnet.fluxdata.org/data/fluxnet2015-dataset/), LaThuile (https://fluxnet.org/data/la-thuile-dataset/), AsiaFlux (http://asiaflux.net/?page_id=23), and OzFlux (https://data.ozflux.org.au/portal/home.jspx) datasets. Following Maes et al. (2019), we processed the four datasets to provide the necessary inputs and the ET observations without water limits (i.e., PET) for calibrating the SW model.

140   First, we screened the measurements using data quality control. Sites lacking one or more of the basic measurements required for our analysis [i.e., latent heat (LE), sensible heat (H), soil heat flux (G), the net radiation fluxes (Rn), wind speed (u), air temperature, and relative humidity (RH)/actual vapour pressure (e_a)/atmospheric water concentration/vapour pressure deficit (D)] were not considered further. Considering potential impacts of surface energy imbalance on the results, the corrected half-hourly or hourly LE and H (Pastorello et al., 2020) were used here. Regarding the major heat fluxes (LE, H and G), good gap-

145   filled records were retained according to the quality flags provided by the four datasets. When the flags for Rn observations were unavailable, the flags of the downward shortwave radiation were used instead. Mainly due to impacts of interception loss and condensation on accuracy of H or LE measurements (Mizutani et al., 1997), the negative values were masked out. Likewise, all Rn negative values were masked out.

Second, the half-hourly or hourly measurements were aggregated to daytime records. Only days in which more than 70% of

150   the basic data were measured directly were retained, and days with rainfall during midnight-sunset were excluded from the analyses for removing the effects of rainfall interception. Moreover, we only retained sites with 80 or more days for the processing below. Taking 5 W/m^2 of top-of-atmosphere incoming shortwave radiation as a minimum threshold, the half-hourly or hourly measurements were aggregated to daytime composites, and then the daytime values were obtained through subtracting measurements at the first and last (half-)hours for these aggregates.

155   Third, we identified days with no soil water limits. This study employed an energy balance-based approach to select unstressed days rather than the soil moisture criterion. The major considerations were three-fold: (a) no soil moisture measurements existed at most of EC sites, (b) the energy balance-based method could effectively remove days in which the ecosystem is not

limited by soil moisture availability but stressed by other environment factors (e.g., insect plagues, phenological leaf-out, fires, heat and atmospheric dryness stress, nutrient limitations), and (c) soil moisture may be not a good indicator of water stress due to variable rooting depth and its inaccurate measurements (Powell et al., 2006; Douglas et al., 2009; Martínez-Vilalta et al., 2014). The evaporative fraction [i.e., $EF = LE/(LE + H)$] was selected as the energy balance criterion, and we assumed that under conditions of no water limits a larger fraction of the available energy should be used for evaporating water (Gentine et al., 2007, 2011; Maes et al., 2011). Taking a site as an example, a day was identified to have no water limits when its corresponding EF exceeded the 95th percentile EF threshold. Notably, if fewer than 15 days fulfilled this criterion at some particular sites, the 15 days with the highest EF were used as unstressed days.

Finally, the sites used for further analyses were selected. Despite usage of the corrected half-hourly or hourly LE and H here, we found that evident surface energy imbalance still existed on daytime with Bowen ratio between 0.60 and 1.80. For further reducing potential impacts of this issue, we retained records with Bowen ratio between 0.90 and 1.10. After this, if a certain site had fewer than 8 unstressed days, it was removed. Because the LAI and CO_2 concentration were unavailable at some sites, the Global LAnd Surface Satellite (GLASS) LAI and CO_2 concentration (ρ_{CO_2}, ppm) observed at Mauna Loa were used instead. At last, 96 sites were retained, including 73, 5, 3 and 18 sites from FLUXNET2015 Tier-2, AsiaFlux, OzFlux, and LaThuile datasets, respectively (Figure 1). Their basic information was shown in Table S1.

2.1.2 Meteorological data

Meteorological inputs are necessary to generate the SW PET, and moreover for reducing uncertainties we collected four monthly or 3-hourly meteorological datasets, i.e., Multi-Source Weather (MSWX)-Past (Beck et al., 2022), National Aeronautics and Space Administration (NASA) Modern Era Reanalysis for Research and Applications (MERRA)-2 (Molod et al., 2015), European Centre for Medium-Range Weather Forecasts Reanalysis (ERA)-5 (Hersbach et al., 2020) and CRUTS4.06 (Harris et al., 2020). The detailed information of these datasets is shown in Table 1. The directly used meteorological variables to drive the SW model mainly include air temperature, u, D, Rn and G. Except for air temperature and u, the meteorological datasets provide different D-related and radiation-related variables (Table 1), and therefore different methods were utilized to estimate D and Rn (details in Texts S1 and S2 and Table S1). Regarding G, the mean air temperature-based method was used here (Allen et al., 1998; details in Text S3). Notably, because the CRU TS4.06 lacked direct radiation records, the algorithm of Reddy (1974) was employed here to estimate Rn based on the Clouds and the Earth's Radiant Energy System (CERES) satellite-based monthly net shortwave radiation records (https://asdc.larc.nasa.gov/project/CERES) and the CRU TS4.06 cloud cover data (algorithm and validation in Text S1 and Figure S1, respectively). Moreover, due to no wind speed records in CRU TS4.06, we used the mean wind speed from the other three meteorological datasets as a proxy.

2.1.3 Land use/land cover, LAI, saturated water content in soil and CO₂ concentration

Considering time span of the available LULC products at present, the 1982–2015 yearly GLASS-Global Land Cover (GLC) dataset developed by Liu et al. (2020) at a spatial resolution of 5000 m was used here, though it has a coarse LULC

190 classification ecosystem (including cropland (CRO), forests (FR), grassland (GRA), shrubland (SHRB), tundra, barren land, and snow/ice). Some studies stated that the accuracy of the GLASS LAI is clearly better than that of others [e.g., Moderate-resolution Imaging Spectroradiometer (MODIS) LAI], especially for forested areas with more realistic and reasonable trajectories representing seasonal variations (Fang et al., 2013; Liang et al., 2013; Xiao et al., 2014, 2016, 2017). Thus, the 1981–2018 8-day GLASS Advanced Very High Resolution Radiometer (AVHRR) LAI product at a spatial resolution of 0.5°

195 was selected in this study (Xiao et al., 2016, 2017). The global saturated water content in soil at the first soil layer (i.e., 0–0.0451 m) and the monthly CO_2 concentration were collected from http://globalchange.bnu.edu.cn/research/soil5.jsp (Dai et al., 2019a, 2019b) and https://gml.noaa.gov/ccgg/trends/data.html (Thoning et al., 2022), respectively.

2.1.4 Vegetation canopy height

To date, the vegetation canopy height (h) maps to fully cover the whole globe still lack, although it is needed for the SW model

200 to estimate some key parameters. Therefore, we made use of the existing datasets, mainly including remote sensing-based forest h datasets of Potapov et al. (2020), Wang et al. (2016), Simard et al. (2011) and Lang et al. (2020, 2022; respectively named as h-Potapov, h-Wang and h-Simard, and h-Lang), and Spatial Production Allocation Model (SPAM) V2.0 crop distribution map (Yu et al., 2020), to reconstruct the global vegetation h maps. For each year, the detailed procedures are four-fold: (1) Mapping FR and SHRB h. For reducing uncertainties related to retrieval algorithms and source data, the h-Potapov,

205 h-Wang, h-Simard and h-Lang datasets were used in this procedure. Notably, we ignored differences in periods of source data for producing the forest h datasets. That is, we assumed that the changes in forest h due to vegetation natural growth were limited during study period. To match GLASS-GLC, the four forest h datasets were firstly resampled to a spatial resolution of 5000 m. If two or more h datasets showed non-missing values at a certain FR (SHRB) grid cell, the average of these non-missing values represented the final h at this grid cell. After this, if some FR (SHRB) grid cells still had missing values, and

210 then the h value at each of these grid cells was filled with the mean h at the four nearest FR (SHRB) grid cells around this grid cell. (2) Mapping GRA and tundra h. Although the h-Lang product provided GRA and tundra h values over few regions, there were still large areas with missing values and even large uncertainties existed (Huang et al., 2017). Therefore, we specified the GRA and tundra h mainly based on the Comprehensive Sequential Classification System (CSCS)-based GRA groups, and the typical GRA and tundra h measured at the EC sites and records from literatures. Using vegetation bioclimate characteristics

215 and hydrothermal indictors (e.g., temperature and precipitation), the CSCS method was employed to classify the GLASS-GLC GRA and tundra into 10 groups (Li and Ma, 2009; Liang et al., 2011; Gang et al., 2016). According to the map of the CSCS-based GRA groups and locations of the EC sites, the h value for each CSCS-based GRA group was estimated as mean h from

the EC sites with such GRA group, and lastly the *h* values for 7 CSCS-based GRA groups were determined. As for the

remaining 3 CSCS-based GRA groups (i.e., frigid desert GRA, warm desert GRA, and tropical zonal forest steppe GRA), their

220 *h* values were from White (1983), Suttie et al. (2005), Kadeba et al. (2015), Yin et al. (2019) and Prakash et al. (2020). The *h*

values of all the CSCS-based GRA groups could be found in Table S2. (3) Mapping CRO *h*. Through overlaying the SPAM

V2.0 and GLASS-GLC maps, the CRO were further classified into 42 types, and the *h* for each type was specified based on

Table S3 (Allen et al., 1998). (4) Mapping *h* of barren land and snow/ice. As for barren land and snow/ice regions, the *h* was

set as 0. The canopy *h* map was shown in Figure S2. Notably, regardless of the *h* map reconstructed at each year, this dataset

225 could not reflect inter-annual variations of *h* except for regions with LULC changes, where the *h* values varied due to LULC

changes.

2.2. Analysis methods

The workflow of this study mainly included three parts (Figure 2): (1) calibrating the SW model based on the identified EC

observations without water limits at 96 EC sites, and validating its performance in site-calibration and cross-validation modes

230 (blue color in Figure 2), (2) generating the global monthly PET using the calibrated SW model with the final r_{smin} values and

various inputs (yellow-green color in Figure 2), and lastly (3) conducing related analyses, i.e., climatological characteristics

and spatio-temporal changes of PET and its two components, and climatological characteristics of PET partitioning (green

color in Figure 2).

2.2.1 Description of the Shuttleworth-Wallace (SW) model

235 Based on assumption that the water vapour arriving at the reference height is a mixture of evaporation from soil and

transpiration from vegetation layer (Shuttleworth and Wallace, 1985, 1990), the SW model can be expressed as:

$$
\begin{cases}
\lambda ET = C_c PM_c + C_s PM_s & (1a) \\
PM_c = \dfrac{\Delta A + (\rho c_p D - \Delta r_a^c A_{soil})/(r_a^a + r_a^c)}{\Delta + \gamma[1 + r_s^c/(r_a^a + r_a^c)]} & (1b) \\
PM_s = \dfrac{\Delta A + [\rho c_p D - \Delta r_a^s (A - A_{soil})]/(r_a^a + r_a^s)}{\Delta + \gamma[1 + r_s^s/(r_a^a + r_a^s)]} & (1c) \\
C_c = [1 + \dfrac{R_c R_a}{R_s(R_c + R_a)}]^{-1} & (1d) \\
C_s = [1 + \dfrac{R_s R_a}{R_c(R_s + R_a)}]^{-1} & (1e) \\
R_a = (\Delta + \gamma)r_a^a & (1f) \\
R_s = (\Delta + \gamma)r_a^s + \gamma r_s^s & (1g) \\
R_c = (\Delta + \gamma)r_a^c + \gamma r_s^c & (1h)
\end{cases}
$$

where λET is the total latent heat flux (W/m²), while *PMc* and *PMs* are the soil and vegetation latent heat fluxes (W/m²),

respectively, which can be calculated by the Penman formulas under conditions of bare soil (i.e., EQ. 1b) and closed canopy

240 (i.e., EQ. 1c); C_c and C_s represent soil surface resistance (i.e., EQ. 1d; unitless) and canopy resistance coefficients (i.e., EQ.

1e; unitless), respectively; *Δ* denotes the slope of the saturated vapor pressure curve (kPa/K); *γ* is the humidity constant (kPa/K);

λ is the latent heat of evaporation (MJ/kg); ρ is the air density (kg/m³); c_p is the constant pressure specific heat (1013 J/kg/K);

r_a^a, r_a^c and r_a^s are the aerodynamic resistance (s/m), the vegetation boundary layer resistance (s/m) and the soil boundary layer

resistance (s/m), respectively; r_s^s is the soil surface resistance, while r_s^c is the vegetation canopy resistance (s/m). In EQs. 1b

245   and 1c, A and A_{soil} are the available energy for canopy and soil layers (W/m²), respectively, and are defined as:

$$\begin{cases} A = R_n - G & (2a) \\ A_{soil} = R_{n,soil} - G & (2b) \\ R_{n,soil} = R_n \exp{(-0.6\text{LAI})} & (2c) \end{cases}$$

where $R_{n,soil}$ is the net radiation fluxes into the soil (W/m²), and can be computed with Beer's Law (i.e., EQ. 2c; Mo et al.,

2004).

Previous studies have stated that determining the five resistance parameters is the key to successfully run the SW model (Hu

250   et al., 2009; Chen et al., 2022). Of these resistance parameters, r_a^a and r_a^s are estimated using Shuttleworth and Gurney (1990),

while r_a^c and r_s^s are calculated based on Shuttleworth and Wallace (1985) and Brisson et al. (1998), and Villagarcía et al. (2010),

respectively. Detailed information about equations for parameterizing the four resistance parameters can be found in Texts S4–

6 and Table S4. Considering large uncertainties of r_s^c (Fisher et al., 2005; Hu et al., 2009, 2013; Wei et al., 2020), this study

used the EC measurements to calibrate its value for each LULC type, and the detailed procedures can be found in section 2.2.2.

255   **2.2.2 Determination of canopy resistance (r_s^c)**

In this study, the parameterization of r_s^c is mainly based on a Jarvis-type model, which is based on the hypothesis that stomatal

resistance is independently affected by every environmental variable (Jarvis, 1976; Shuttleworth and Wallace, 1985). Here, we

considered effects of LAI, D, air temperature (T, ºC), soil moisture and ρ_{CO2} on r_s^c, which correspond to stress functions of F_1

(Noilhan and Planton, 1989), F_2 (Raab et al., 2015), F_3 (Zhou et al., 2005), F_4 and F_5 (Neitsch et al., 2002). Notably, this study

260   focuses on ET under condition with no soil water limits (namely PET), and thus F_4 is set to 1 here. The specific equations are

shown as follows:

$$\begin{cases} r_s^c = \dfrac{r_{smin}}{LAIe \prod_{i=1}^{N=5} F_i} & (2a) \\[2mm] LAIe = \begin{cases} \text{LAI}, & \text{LAI} \le 2 \\ 2, & 2 < \text{LAI} < 4 \\ \text{LAI}/2, & \text{LAI} \ge 4 \end{cases} & (2b) \\[4mm] F_1 = \dfrac{0.55 \dfrac{R_{ds}}{R_{ds,dbl}} \dfrac{2}{\text{LAI}} + \dfrac{r_{smin}}{r_{smax}}}{0.55 \dfrac{R_{ds}}{R_{ds,dbl}} \dfrac{2}{\text{LAI}} + 1} & (2c) \\[4mm] F_2 = \exp(-0.5D) & (2d) \\ F_3 = 1 - 0.0016(24.84 - T)^2 & (2e) \\ F_4 = 1 & (2f) \\ F_5 = 1 + \left(1 - \dfrac{\rho_{CO2}}{330}\right) \Delta g_{1,CO2} & (2g) \end{cases}$$

where r_{smin} represents the minimum canopy resistance (m/s); r_{smax} is the maximum canopy resistance (s/m), and is fixed at 5000

s/m here (Crow et al., 2008); $LAIe$ denotes the effective LAI (Gardiol et al., 2003); R_{ds} is the downward shortwave radiation

265   (W/m2); $R_{ds,dbl}$ is the minimum shortwave radiation threshold for vegetation to carry out photosynthesis (W/m²), which is set

to 30 W/m² for forests and 100 W/m² for other vegetation (Noilhan and Planton, 1989; Lo Seen et al., 1997); $\Delta g_{1,CO2}$ is the

multiple of leaf stomatal conductance reduction when ρ_{CO2} is doubled (Table S1; Morison and Gifford, 1984; Field et al., 1995;

Saxe et al., 1998; Neitsch et al., 2002; Eckhardt and Ulbrich, 2003; Wu et al., 2017).

Finally, we determined the values of r_{smin}. Here, the Monte Carlo method was used to calibrate this parameter using the

270   identified PET observations at each EC site (Hu et al., 2009). The following five steps were taken to determine the r_{smin} values:

(1) giving a rough range for r_{smin} (i.e., r_{smin} between 1 s/m and 500 s/m) with references to previous studies (e.g., Zhou et al.,

2006; ECWMF, 2007), (2) conducting 5,000 Monte Carlo simulations with the parameter sets randomly sampled from uniform

distributions within the given ranges, (3) comparing the estimated SW model-based PET (SW PET) and the EC PET after each

simulation based on a validation metric of the Kling-Gupta Efficiency (*KGE*; seen EQ. 3d; Gupta et al., 2012; 5,000 parameter

275   sets corresponded to 5,000 *KGE* after this step), (4) selecting the mean of r_{smin} with the 10 highest *KGE* as the optimal value

for each site, and (5) classifying the 96 EC sites into 4 types (i.e., FR, SHRB, CRO and GRA) based on the GLASS-GLC

classification system (Liu et al., 2020), and then determining the best-fit parameter sets for a given LULC type through

averaging the optimal parameter values at the sites with this LULC type. In this way, the final parameter values for FR, CRO,

GRA and SHRB were obtained and illustrated in Table S5. Notably, the r_{smin} for tundra, barren land and snow/ice types of the

280   GLASS-GLC are from Zhou et al. (2006) and Zhang et al. (2008), mainly due to lack of the corresponding EC observations.

2.2.3 Model validation

Several validation metrics were employed to evaluate the performance of the simulated SW PET. Mean error (*ME*) provides a

way to quantify the biases of the estimates relative to measurements, while unbiased Root-Mean-Square-Error (*unRMSE*)

describes the accuracy of estimations. Besides, correlation coefficient (*R*) and *KGE* [with a range between -∞ and 1.0 (the

285   optimal value)] were used to measure capability of capturing the spatio-temporal variability and the overall performance of

the SW PET, respectively. The metrics are expressed as:

$$ME = \frac{\sum_{i=1}^{N}(S_i - O_i)}{N} \tag{3a}$$

$$unRMSE = \sqrt{\frac{\sum_{i=1}^{N}[(S_i - S) - (O_i - O)]^2}{N}} \tag{3b}$$

$$R = \frac{\sum_{i=1}^{N}[(S_i - S)(O_i - O)]}{\sqrt{\sum_{i=1}^{N}(S_i - S)^2 \sum_{i=1}^{N}(O_i - O)^2}} \tag{3c}$$

$$KGE = 1 - \sqrt{(1 - R^2) + (1 - \alpha^2) + (1 - \beta^2)} \tag{3d}$$

where *N* is the sample number; *S* denotes the mean of the SW PET averaged *N* samples; *O* is for the measured PET; *i* is the *i*th

sample; α is S/O; β is σ_S/σ_O, where σ_S and σ_O are the standard deviations of the estimated and the measured PET, respectively.

290   These metrics were first computed based on the daily estimates with the optimal parameters for each site [i.e., parameters

obtained in step (4) of the Monte Carlo method] and the observations from the 96 EC sites, and then validation in site-

calibration mode was performed. Notably, to evaluate the transferability of the calibrated parameters from known observations to any location and then robustness of the established SW model, the "leave-one-out" cross-validation method was utilized here (Zhang et al., 2019). For each LULC type, the data from one "ungauged" observation was excluded from the Monte Carlo

295   method-based optimization while the data from all other observations of the same LULC type were used for model calibration to obtain the simulated at the "ungauged" position. All four LULC types were actualized in this way. Then, the daily SW PET estimates in the cross-validation mode were compared against the daily observations from the 96 EC sites to further explore the model performance.

2.2.4 Development of 5 km global monthly PET (1982–2015) and related analyses

300   The global SW PET was produced at GLASS-GLC grid and monthly scale during 1982–2015 (mainly due to the GLASS-GLC with the shortest time span). Therefore, before running the calibrated SW model, the meteorological and the GLASS LAI datasets were resampled to a spatial resolution of 5000 m. The monthly mean meteorological and LAI datasets were taken as inputs to run the calibrated model for estimating the monthly mean SW PET, PT and PE. At last, the total SW PET (PT and PE) at a certain month were obtained through monthly mean value multiplying days of this month. Additionally, to reduce

305   uncertainties from meteorological datasets, the ensemble means of PET, PT and PE based on four meteorological datasets were provided. Using the ensemble mean PET, PT and PE, we analyzed climatological characteristics and spatio-temporal changes of PET and its two components, and climatological characteristics of PET partitioning.

3. Results

3.1 Performance of established SW model

310   The simulated daily PET from the SW model was first evaluated against EC measurements aggregated for all of 96 EC sites (Figures 3a and 3c). In both site-calibration and cross-validation modes, the SW model could well simulate the daily PET with most of data points around the 1:1 line, while it should be noted that overestimation and underestimation existed for the lower and the higher measurements, respectively (Figure 3a). Based on the selected validation metrics, we could conclude that the model had excellent performance in the two modes, with R, ME, $unRMSE$ and KGE values above 0.85, between -0.03 and 0.01

315   mm/day, below 0.80 mm/day and above 0.85, receptively. Regarding the mean values of each site (Figures 3b and 3d), the simulated daily PET could also well follow changes of the observed PET among 96 sites in both modes, as evidenced by R above 0.88, ME between -0.06 and -0.03 mm/day, $unRMSE$ below 0.88 mm/day and KGE above 0.87. Moreover, little changes in the validation metrics from site-calibration to cross-validation indicated limited degradation of the calibrated model (i.e., Figure 3a vs. 3c, and Figure 3b vs. 3d).

320   Figure 4 indicates that in site-calibration and cross-validation modes the SW model estimated daily PET very well for FR,

SHRB, GRA and CRO. The model slightly overestimated lower daily PET but slightly underestimated higher daily PET. The performance of this model slightly differed among LULC types. R was above 0.84, indicating that the model could successfully simulated spatio-temporal variability of the daily PET, especially for FR, SHRB and GRA in site-calibration mode. Although negative and positive ME existed in CRO and GRA and the other two LULC types, respectively, the ME magnitudes were all

325   below 0.15 mm. According to $unRMSE$, the simulated GRA daily PET performed best in each mode, while larger values (> 0.70 mm/day) occurred in other three LULC types, especially for CRO in site-calibration mode and SHRB in cross-validation mode. The KGE was always larger than 0.80 for each LULC type in site-calibration and cross-validation modes, which indicated that the calibrated model overall had a high performance. When it came to validation based on site mean values, the simulated PET well followed changes of the observed PET for each LUCC type in the two modes, with R above 0.75, ME

330   between -0.11 and 0.11 mm, $unRMSE$ below 0.70 mm and KGE above 0.74. For each LULC type, the cross-validation mode had slightly lower performance than the site-calibration mode (Figure 4a vs. 4e, Figure 4b vs. 4f, Figure 4c vs. 4g, and Figure 4d vs. 4h).

For further evaluating the performance of the established SW model, we also computed the validation metrics at each site for each LULC type in site-calibration and cross-validation modes, which are shown in Figure 6. Except for several sites for FR

335   and CRO, the R values were all above 0.80 and more than 50% of the sites had a value above or around 0.90, which indicated that the model had excellent performance in capturing the temporal variability of daily PET (Figure 6a). As for ME, the majority of the sites for each LULC type showed a range between -0.50 mm and 0.50 mm (Figure 6b). Moreover, the daily PET for SHRB (other three LULC types) was overestimated (underestimated) by the SW model at more than 50% of the sites. Except for few sites, the $unRMSE$ values were below 0.80 mm at more than 75% of the sites for each LULC type, and comparably the

340   $unRMSE$-based performance for SHRB was the worst generally with $unRMSE$ above 0.50 mm (Figure 6c). The majority of the sites had a KGE value above 0.60, and especially for GRA and CRO, more than 75% of the sites had KGE larger than 0.70 (Figure 6d). In general, the model performance in the cross-validation model was similar to only slightly lower than that in the calibration model for each LULC type.

To sum up, the above evaluation indicated that the calibrated parameter of r_{smin} could be transferable from known observations

345   to any location and then the established SW model could well simulate PET across different LULC types. This gave us confidence to employ it to produce a global PET dataset. Notably, for maximizing data utilization, the final values of r_{smin} for each LULC type were determined based on all the EC observations (Table S5), and the related validation results could be found in Figure S3.

3.2 Climatological characteristics of PET, PT and PE

350   As seen from Figures 7a, 7d and 7g, the global mean climatological annual PET, PT and PE were 1200 mm, 472 mm and 728 mm, respectively. Compared to Northern Hemisphere (NH), larger mean climatological annual PT and thus PET appeared in

Southern Hemisphere (SH) where a larger proportion of the land surface was covered by vegetation. Among the five KG climate regions, mean climatological annual values of PET and its two components showed evident differences, with a range from 319.47 mm in Polar region to 1595.94 mm in Tropical region for PET, from 37.75 mm in Polar region to 1105.88 mm in

355   Tropical region for PT, and from 253.46 mm in Cold region to 1384.71 mm in Arid region for PE. Except for the Tibetan Plateau with a lower value, climatological annual PET was generally larger than 1000 mm between 60ºS and 45ºN, covering 62% of the globe (Figure 7b). Especially, climatological annual PET exceeded 1800 mm over northern Africa, Arabian Peninsula, Indian Peninsula, Indo-China Peninsula and northern Australia. The lowest climatological annual PET (< 400 mm) was generally located to the north of 60ºN. As seen in Figure 7e, the spatial distribution of climatological annual PT differed

360   from that of climatological annual PET. Due to sparse and even no vegetation and/or unfavorable climate conditions, lower climatological annual PT (< 400 mm) was widely distributed to the north of 18ºN and to the south of 18ºS, corresponding to an area percentage of 55%. By contrast, 16% of the globe with larger climatological annual PT (> 1200 mm) was mainly located in Caribbean, Amazon Basin, Congo Bains and Indo-China Peninsula. As for climatological annual PE, larger values (> 1000 mm) were generally clustered in northwestern North America and South America, northern Africa, western Asia and

365   most of Australia, which corresponded to sparse and even no vegetation and covered 36% of the globe. Notably, lower climatological annual PE (< 400 mm) appeared in tropical rain forests near the Equator, possibly because the dense vegetation limited available energy for PE (Figure 7h).

As expected, climatological monthly PET, PT and PE generally exhibited strong seasonal fluctuations because of the combined influences from many environmental factors (Figure 8). The globe and NH showed a similar seasonal cycle for climatological

370   monthly PET, PT and PE, i.e., increasing from January, peaking in July, and afterwards declining, while an opposite seasonal fluctuation existed in SH with a valley in June (Figures 8a–c). Mainly due to differences in environmental factors, the seasonal cycles of climatological monthly PET, PE and PT obviously differed among various KG climate regions (Figures 8d–h). As for Tropical region, no evident seasonal fluctuations existed for the three variables, which slightly fluctuated around 136 mm, 88 mm and 40 mm, respectively (Figure 8d). In Arid, Cold and Polar regions, climatological monthly PE, PT and PE were

375   characterized by a peak in July or August (Figures 8e, 8g, and 8h), while Temperate region showed larger values in April–November (Figure 8f).

3.3 Climatological characteristics of PET Partitioning

In order to know PET partitioning, we estimated the ratios of PT and PE to PET (i.e., PT/PET and PE/PET) at annual and monthly scales (Figures 8 and 9). As depicted in Figures 9a and 9c, the global mean annual PT/PET and PE/PET were 40%

380   and 60%, respectively, indicating that globally the annual PE greatly contributed to the annual PET. Likewise, the annual PE was also the major contributor in NH and SH, with the PE/PET of 63% and 51%, respectively. Overall, the annual PT/PET (PE/PET) had evident regional differences, and was above 52% (below 47%) in Tropical, Temperate and Polar regions but

below 12% (above 88%) in other two climate regions (Figures 9a and 9c). These indicated that the annual PET in Tropical, Temperate and Polar regions (Arid and Cold regions) was controlled by PT (PE). Spatially, the annual PE/PET was above 50%

385   mainly in regions to the north of 65°N, western North America, the Patagonia and the Andes of South America, western and central Asia, northern and southern Africa, and Australia (Figure 9c), while the remaining regions showed PT/PET larger than 50%, especially for Amazon Basin, Congo Basin and southeastern Asia with a value exceeding to 90%. Compared to the annual PT/PET, the annual PE/PET corresponded to an opposite spatial distribution (Figure 9d). In short, the annual PET was dominated by PE and PT over 60% and 40% of the globe, respectively.

390   In general, the seasonal cycle of PT/PET (PE/PET) for the globe, each hemisphere, and each KG climate region was different from that of PT (PE; Figure 8). As for the globe, NH and Polar region (Figures 8a, 8b and 8h), the monthly PT/PET had two bottoms in April and October and a peak in July, corresponding to tow peaks and a bottom of the monthly PE/PET. In SH and Temperate (Cold region), the monthly PT/PET firstly increased from January, peaked in July (June), and after that declined, while the monthly PE/PET showed opposite fluctuations (Figures 8c, 8f and 8g). No evident fluctuations of the monthly

395   PT/PET and PE/PET existed in Tropical and Arid regions (Figures 8d and 8e). Comparing the monthly PT/PET and PE/PET in the globe, NH, Arid region and Polar region (Figures 8a, 8b, 8e and 8h), it was not difficult to find that the former was always smaller the latter, indicating that the monthly PE greatly contributed to the monthly PET. Oppositely, the larger monthly PT/PET in Tropical and Temperate regions suggested that PT dominated PET in these regions (Figures 8d and 8f). In particular, the major contributor to the monthly PET for SH (Cold region) varied throughout a year, i.e., PT dominating PET in March–

400   July (May–September) but PE dominating PET in other months (Figures 8c and 8g).

3.4 Spatio-temporal changes in PET, PT and PE

Globally, annual PET and PT significantly ($p<0.05$) increased by 1.25 mm/yr and 1.22 mm/yr, respectively, with a slight and insignificant increase in annual PE (Figures 10a-c). Regarding annual PET and PT, both NH and SH had significant ($p<0.05$) increases, while annual PE oppositely changed in the two hemispheres, i.e., increases for NH but decreases for SH (Figures

405   10b and 10c). Among various KG climate regions, annual PET (except for Tropical region) and PT were all found to significantly ($p<0.05$) increase but with evident regional differences in magnitudes, i.e., larger PET increases (>1.36 mm/yr) in Arid, Temperate and Cold regions and a maximum increase (1.84 mm/yr) in PT in Temperate region (Figures 10a–c). Except for Polar region, the other climate regions all showed significant ($p<0.05$) changes in annual PE, followed by decreases in Tropical and Temperate regions but increases in Arid and Cold regions. Comparisons between annual trends of PT and PE

410   suggested that the increases in PET could be attributed to increased PT for the globe, each hemisphere and each climate region. Spatially, increases in annual PET covered 78% of the globe, accompanied by 41% of the globe with significant ($p<0.05$) increases and larger values (>4.00 mm/yr) in western US, Amazon Basin, Congo Basin, eastern Europe and eastern China (excluding northeastern part; Figure 10d). As for annual PET, only 5% of the globe had significant ($p<0.05$) reductions. No

considering non-vegetation regions, the spatial pattern of annual PT trends was similar to that of annual PET trends (Figure

415   10e). Overall, significant ($p<0.05$) increases and decreases in annual PT were observed for 28% and 4% of the globe,

respectively, especially for Amazon Basin, Congo Basin, southern Africa, Indian Peninsula, eastern Europe and eastern China

(excluding northeastern part) with larger increases exceeding to 4.00 mm/yr. As shown in Figure 10f, the increasing trends of

annual PE had a wide distribution but significant ($p<0.05$) increases only covered over 26% of the globe and the increases

were generally below 3.00 mm/yr. Relative to annual PET and PT, annual PE had more regions showing decreases, with

420   significant ($p<0.05$) reductions over 13% of the globe mainly in northern South America and Australia, southern Africa, and

Indian Peninsula. In general, the spatial distribution of major contributors to annual PET trends was similar to that of major

contributors to annual PET (Figure 10g vs. Figures 9b and 9d). For example, the major contributor of PE was mainly located

in Greenland, southwestern North America, the Patagonia and the Andes of South America, western and central Asia, northern

and southern Africa, and most of Australia (Figure 10g). Oppositely, the remaining regions showed the dominant factor of PT.

425   Overall, the annual PET changes were dominated by PT and PE over 53% and 47% of the globe, respectively.

In general, the globe mean monthly PET and PT significantly ($p<0.05$) increased throughout a year with larger trends (> 0.10

mm/yr) during April–October, while the global mean monthly PE insignificantly changed in each month (Figure 11a). For NH

(Figures 1b), all months showed significant ($p<0.05$) increases in PET and PT, especially for March–September with trends

generally larger than 0.10 mm/yr. Despite most of months with increased PE, only March had significant ($p<0.05$) increases

430   in NH. In SH (Figure 11c), monthly PET showed larger (> 0.10 mm/yr) and significant ($p<0.05$) increases during June–October

but decreases in other months. The SH PT significantly ($p<0.05$) increased in most of months, with larger values (> 0.12 mm/yr)

during August–October. As for the SH PE, June–October, and January–March and December corresponded to significant

($p<0.05$) increases and reductions, respectively. Among the five KG climate regions (Figures 11d–h), the monthly PET and PT

increased throughout a year except for PET of Tropical region in several months with decreases, and moreover the increases

435   in most of months were significant ($p<0.05$). When it came to the monthly PE changes, most of or all months exhibited

decreases in Tropical and Temperate regions but increases in other three KG climate regions. Despite that, no more than 6

months exhibited significant ($p<0.05$) increases or decreases in the monthly PE for each climate regions. Furthermore, we

compared trends of the monthly PT and PE for identifying major contributors to the monthly PET changes of the globe, each

hemisphere, and each KG climate region (Figure 11). Overall, the monthly PET changes were generally dominated by PT in

440   most of or all months for the globe and each region. However, it should be noted that PE was the major contributor of PE for

some months, i.e., January–March for SH, March and December for Cold region, and February–May, October and November

for Polar region.

4. Discussion

4.1 Advantages of this new PET dataset and its potential implications

445   Through comprehensively considering the joint effects of various ET process-related factors, we have developed a new global gridded dataset of PET based on the SW model. This dataset has several advantages relative to existing global PET datasets, e.g., CRU TS4.06 (Harris et al., 2020), MOD16 (Running et al., 2017), Global Land Evaporation Amsterdam Model (GLEAM) v3.6 (Miralles et al., 2011; Marten et al., 2017), Priestly-Taylor Jet Propulsion Laboratory (PT-JPL) Model (Fisher et al., 2011), and hPET (Singer et al., 2021). First, we considered more realistic land surface and relevant parameters in this study, including

450   spatial differences in LULC and vegetation parameters (e.g., canopy height and r_{smin}), and time-varying LULC and LAI datasets. Thus, this new dataset could provide more realistic PET estimates. Second, the more physically-based SW model used for estimating PET indicated that the SW PET dataset had explicit physical significance, and moreover two important components (PT and PE) of PET were also provided, which are crucial for physically understanding in PET and then ET processes. Third, a number of studies have found that the elevated atmospheric CO_2 concentration could exert great impacts on ET process through controlling plant stomatal resistance (Gedney et al., 2006; Piao et al., 2007; Sun et al., 2014; Roderick et al., 2015;

455   Milly and Dunne, 2016; Yang et al., 2019; Zhao and Cao, 2022), and therefore the SW PET dataset is able to reflect impacts of elevated CO_2 on ET process through introducing a stress function of CO_2 concentration on r_s^c.

In view of these advantages, our global, gridded PET dataset can be useful for many applications, e.g., rainfall, agriculture, drought, hydrology and biodiversity. First, our SW PET can provide more realistic and physical datasets to further understand

460   the spatio-temporal differences in rainfall changes from perspective of scaling effects of the Clausius-Clapeyron relation between air temperature and moisture-holding capacity (IPCC, 2014; Barbero et al. 2017). For example, through exploring the relationships between evaporative demand (even PT and PE) and rainfall, one can re-untangle different scaling effects of the Clausius-Clapeyron relation between air temperature and moisture-holding capacity. Second, considering PET partitioning into two components of PT and PE, this dataset will be convenient for the agriculture managers to directly use PT estimates

465   for effective agricultural management practices (e.g., seeding, fertilization, irrigation planning and scheduling) and finally for sustaining the grain yield (Allen et al., 1998; Tomas-Burguera et al., 2019). Third, our SW PET dataset provides an opportunity to further understand drought mechanisms, e.g., how and what magnitudes different PET components (i.e., PT and PE), LULC changes, vegetation greening and elevated CO_2-indcued vegetation physiological effects (e.g., increased stomatal resistance) impact droughts, which are still unclear until now (Vicente-Serrano et al., 2020). One can use this dataset as inputs to compute

470   drought indices [i.e., Standardized Precipitation-Evapotranspiration Index (SPEI) and self-calibrating Palmer Drought Severity Index (scPDSI); Wells et al., 2004; Vicente-Serrano et al., 2010], and separate the impacts of the aforementioned factors on drought evolution. Fourth, the PET as a crucial input for many hydrological models is closely related to performance of these models (Lu et al., 2003, 2005; Rao et al., 2011; Aouissi et al., 2016; Seiller and Anctil, 2016; Dallaire et al., 2021), and therefore

more realistic and physical PET estimates (i.e., our datasets) benefit for accurate hydrological modellings and physically

475   understanding hydrological responses to environment changes (e.g., changes in climate and LULC). Fifth, the new PET dataset

is of significance for understanding biodiversity responses to local environment changes (including changes in LULC and

vegetation), because this variable usually as an effective measure of climatic energy limits organisms directly and/or influences

primary productivity and thus food availability (Kerr, 2001; Hawkins et al., 2003; Phillips et al., 2010).

4.2 Uncertainties

480   The estimated SW PET may involve uncertainties from various sources, such as parameterizations of the SW model and inputs

for calibrating and driving the model. These uncertainties are discussed in the following sections.

4.2.1 Uncertainties in parameterizations of the SW model

A relatively simple Jarvis-type empirical formula was employed here to describe the impacts of environmental conditions (i.e.,

temperature, vapor pressure deficit, solar radiation, soil moisture content and CO_2 concentration) on r_a^c. Whereas the better

485   performance of the Jarvis-type formula in simulating the impacts of environmental conditions on water and carbon fluxes

(Jarvis, 1976; Lhomme, 2001; Wang et al., 2020), the interactive effects between environmental factors on r_a^c are not taken

into account by this empirical formula. In reality, environmental factors are interdependent and hence their interaction in the

Jarvis-type empirical formula cannot be easily separated. In one word, the "multiplication" form of the Jarvis-type empirical

formula potentially biases the estimated r_a^c (Damour et al., 2010; Chen et al. 2022) and then the SW PET estimates.

490   As an important and undetermined parameter within the Jarvis-type empirical formula for estimating r_a^c, r_{smin} was optimized

for FR, SHRB, GRA and CRO and the calibrated SW model performance was satisfactory (details in section 3.1). However, it

should be noted that this optimized parameter may be the main hindrance for the SW model application over the globe (Liu et

al., 2003; Mo et al., 2004; Chen et al., 2022). First, r_{smin} was estimated using EC observations that generally cover the period

after 2000 assuming stationary environment conditions. Environment conditions were evidenced to have greatly changed

495   during the past several decades, especially climate conditions, such as global warming (IPCC, 2014), brightening/dimming

(Wild, 2009) and frequent extreme events (e.g., droughts; Sheffield et al., 2012; Trenberth et al., 2012). Therefore, r_{smin} may

have inter-annual variations due to the changes in these variables (Wever et al., 2002; Winkel et al., 2001), and this finally

introduces biases into the PET product, particularly for years with evidently different environment conditions relative to the

period after 2000 (Aschonitis et al., 2017). Second, r_{smin} was fixed throughout the year in the SW model, regardless of seasonal

500   variations of this parameter with environmental and vegetation conditions (Winkel et al., 2001; Wever et al., 2002; Douglas et

al., 2009). Therefore, no consideration of seasonal cycle of r_{smin} may impact the quality of the PET product (Hu et al., 2009;

Zhu et al., 2013; Elfarkh et al., 2021). For instance, Hu et al. (2009) and Zhu et al. (2013) found that ET was systematically

overestimated or underestimated using the SW model with fixed parameters.

Noteworthily, the SW model only focuses on two processes of ET, namely soil evaporation and vegetation transpiration

505 (Shuttleworth and Wallace, 1985). Another part of ET, vegetation canopy interception is ignored in this study, although it can

occupy a certain proportion in total ET, especially for regions with high LAI and frequent rainfall (Gash et al., 1995; Tourula

and Heikinheimo, 1998; Lawrence et al., 2007; Wang and Dickinson, 2012). On rainy days, the vegetation canopy interception

may account for a considerable fraction of the total ET (Tourula and Heikinheimo, 1998; Hu et al., 2009). Undoubtedly,

ignoring vegetation canopy interception may underestimate PET (Tourula and Heikinheimo, 1998; Lawrence et al., 2007; Mu

510 et al., 2011). Subsequent research will be done to integrate the vegetation interception process in the SW model to further

enhance the model's physical mechanism.

4.2.2 Uncertainties in datasets for calibrating and driving the SW model

The uncertainties in the EC observations for calibrating the SW model and in inputs for producing the global PET can be

propagated into the PET estimates. As for the EC observations, the uncertainties mainly come from the selection of unstressed

515 days for obtaining the observed PET and issue of non-closure of the energy balance at the EC system level. The energy balance-

based criterion employed in this study was proved to be efficient to select unstressed days (Maes et al., 2019), but we should

note the fact that the higher the LAI/Normalized Difference Vegetation Index (NDVI) is, the larger the EF will be (Gentine et

al., 2007; Nutini et al., 2014). This suggests that the larger EF would like to frequently happen during the growing season,

which usually correspond to higher LAI/NDVI. Therefore, the identified unstressed days tended to involve less ones within

520 non-growing season, potentially introducing large biases in estimated PET during this season. In order to reduce impacts of

non-closure of the energy balance at the EC system level on our study (Wilson et al., 2002; Foken, 2008), we used the corrected

half-hourly or hourly EC LE and H observations and only retained daytime records with Bowen ratio between 0.90 and 1.10

to calibrate the SW model. Although such processing could reduce uncertainties, the energy imbalance issue was not essentially

solved here and may lead to inevitable errors in the calibrated parameter of r_{smin} and lastly the global PET estimates (Hu et al.,

525 2009; Elfarkh et al., 2020; Chen et al., 2022).

The SW model used various datasets as inputs, including LULC, LAI, canopy height and meteorological data (e.g., MSWX-

Past, CRU TS4.06, ERA5 and MERRA-2), in which some uncertainties exist (Fang et al., 2013; Xiao et al., 2017; Liu et al.,

2018; Xu et al., 2018). As a critical variable describing vegetation condition, the accuracy of LAI can affect several key

parameters (e.g., r_a^c, r_s^c, r_a^a, and r_a^s) and input variables (e.g., A and A_{soil}) and further affects quality of the PET estimates. To

530 reduce uncertainties from LAI datasets, this study selected the GLASS AVHRR LAI product with a better overall performance

(relative to other popular products, e.g., MODIS, FSGOM, GLOBMAP and GIMMS3g; Fang et al., 2013; Xiao et al., 2017;

Liu et al., 2018; Xu et al., 2018). However, we should note that the performance of this LAI product was slightly unsatisfactory

in grassland plots compared to other products (Liu et al., 2018). Considering impacts of LULC changes on PET across the

globe, we used the 1982–2015 yearly GLASS-GLC dataset developed by Liu et al. (2020) to separately estimate PET for each

535   LULC type. Although the average overall accuracy for the 34 years each with seven classes is 83% based on 2431 test sample units, misclassification issues still existed, e.g., Africa, eastern and southern South America, southern Alaska, northern and eastern Australia and south-western Indonesia (Liu et al., 2020). The reconstructed global vegetation canopy height has some limitations, which may come from (1) uncertainties of retrieval algorithms and remote sensing data (Simard et al., 2011; Wang et al., 2016; Potapov et al., 2020; Lang et al., 2021, 2022), (2) neglect of spatial differences in CRO and GRA heights to use a

540   specific value instead, and (3) no consideration of inter-annual changes of FR and SHRB canopy heights and intra-annual cycle of CRO and GRA heights. Finally, these limitations exerted adverse impacts on accuracy of the PET estimates. A series of evaluations of various meteorological datasets across the world suggested evident discrepancies among these datasets, especially for some regions and for specific meteorological variables (e.g., Urraca et al., 2018; Hinkelman, 2019; Jourdier, 2020; Zhang et al., 2021). Although the ensemble mean method used here could partly reduce uncertainties from the

545   meteorological datasets, the remaining uncertainties would likely propagate into the PET estimates.

5 Conclusions

This study developed a global 5 km monthly PET dataset during 1982–2015 using the calibrated SW model. The model has been well-calibrated against observations at 96 EC flux sites across four major LULC types: forests, shrubland, cropland, and grassland. We mapped spatio-temporal changes in PET and its components (i.e., PT and PE) across the globe.

550   Our PET product has three major improvements relative to the existing PET datasets: (1) it provides more realistic PET estimates, because spatial differences and temporal changes of land surface properties are considered, (2) it includes not only PET estimates but also PT and PE, and moreover (3) it can reflect impacts of elevated CO_2 on PET through introducing the stress function of CO_2 on r_s^c. This dataset can be used by various scientific disciplines (e.g., agronomy, ecology, climatology, hydrology and so on) and policy makers for different operational applications.

6 Data availability statement

555

The product named SW PET with monthly and 5 km resolutions from 1982 to 2015 is freely available at the National Tibetan Plateau Data Center (https://doi.org/10.11888/Terre.tpdc.300193, Sun et al., 2023).

Author contributions

SS and ZB designed the research. ZB, YL and XL collected the EC observations and other input data. JX, YL, GS, WJ, CL,

560   MM, JL, YZ, and HC revised the paper.

Competing interests

The authors declared that they have no conflict of interest.

Acknowledgments

This work was jointly supported by the National Key Research and Development Program of China (Grant No.
2022YFF0801603), National Natural Science Foundation of China (Grant NOs. 42075189 and 42130609), and Natural Science
Foundation of Sichuan Province of China (2022NSFSC0215). We thank the data developers, their managers, and funding
agencies, whose work and support were essential to data access. The source code for the model used in this study and input
files necessary to reproduce the simulations is available from the authors upon request (sun.s@nuist.edu.cn).

References

Allen, R. G., Pereira, L. S., Raes, D. and Smith, M.: Crop Evapotranspiration: Guidelines for computing crop water
requirements, Irrigation and Drainage Paper 56, Food and Agriculture Organization of the United Nations, Rome, 1998.

Aouissi, J., Benabdallah, S., Chabaâne, Z. L., and Cudennec, C.: Evaluation of potential evapotranspiration assessment
methods for hydrological modelling with SWAT—Application in data-scarce rural Tunisia. Agricultural Water Management,
174, 39–51, 2016.

Aschonitis, V. G., Papamichail, D., Demertzi, K., Colombani, N., Mastrocicco, M., Ghirardini, A., Castaldelli, G. and Fano, E.
–A.: High-resolution global grids of revised Priestley-Taylor and Hargreaves-Samani coefficients for assessing ASCE-
standardized reference crop evapotranspiration and solar radiation. Earth System Science Data, 9, 615–638, 2017.

Aschonitis, V. G., Demertzi, K., Papamichail, D., Colombani, N. and Mastrocicco, M.: Revisiting the Priestley-Taylor method
for the assessment of reference crop evapotranspiration in Italy. Italian Journal of Agrometeorology, 20, 5–18, 2015.

Barbero, R., Fowler, H. J., Lenderink, G. and Blenkinsop, S.: Is the intensification of precipitation extremes with global
warming better detected at hourly than daily resolutions? Geophysical Research Letters, 44, 974–983, 2017.

Beck, H. E., Zimmermann, N. E., McVicar, T. R., Vergopolan, N., Berg, A., and Wood, E. F.: Present and future Köppen-
Geiger climate classification maps at 1-km resolution. Scientific Data, 5, 180214, 2018. https://doi.org/10.1038/sdata.2018.214

Berengena, J. and Gavilán, P.: Reference evapotranspiration estimation in a highly advective semiarid environment. Journal of
Irrigation and Drainage Engineering, 131, 147–163, 2005.

Beven, K.: Rainfall-runoff modelling. The primer, 2nd Edn., John Wiley & Sons Ltd, Oxford (UK), 457 pp., 2012.

Brisson, N., Itier, B., L'Hotel, J. C. and Lorendeau, J. Y.: Parameterisation of the Shuttleworth-Wallace model to estimate daily
maximum transpiration for use in crop models. Ecological Modelling, 107, 159–169, 1998.

Brisson, N., Ltier, B., L'Hotel, J. C. and Lorendeau, J. V.: Parameterisation of the Shuttleworth-Wallace model to estimate

590   daily maximum transpiration for use in crop models. Ecological Modelling, 107(2–3), 159–169, 1998.

Chen, C., Park, T., Wang, X., Piao, S., Xu, B., Chaturved, R. K., Fuchs, R., Brovkin, V., Ciacis, P., Fensholt, R., Tømmervik, H., Bala, G., Zhu, Z., Nemani, R. R. and Myneni, R. B.: China and India lead in greening of the world through land-use management. Nature Sustainability, 2, 122–129, 2019.

Chen, H., Jiang, A. Z., Huang, J. J., Li, H., McBean, E., Singh, V. P., Zhang, J., Lan, Z., Gao, J. and Zhou, Z.: An enhanced
595   Shuttleworth-Wallace model for simulation of evapotranspiration and its components. Agricultural and Forest Meteorology, 313, 108769, https://doi.org/10.1016/j.agrformet.2021.108769, 2022.

Crow, W. T. and Kustas, W. P.: Monitoring root-zone soil moisture through the assimilation of a thermal remote sensing-based soil moisture proxy into a water balance model. Remote Sensing of Environment, 112(4), 1268–1281, 2008.

Dai, Y., Wei, N., Yuan, H., Zhang, S., Shangguan, W., Liu, S., Lu, X. and Xin, Y.: Evaluation of soil thermal conductivity
600   schemes for use in land surface modelling. Journal of Advances in Modeling Earth Systems, 11(11), 3454–3473, 2019a.

Dai, Y., Xin, Q., Wei, N., Zhang, Y., Shangguan, W., Yuan, H., Zhang, S., Liu, S. and Lu, X.: (2019b), A global high-resolution dataset of soil hydraulic and thermal properties for land surface modeling. Journal of Advances in Modeling Earth Systems, 11(9), 2996−3023, 2019b.

Dallaire, G., Poulin, A., Arsenault, R., and Brissette, F.: Uncertainty of potential evapotranspiration modelling in climate
605   change impact studies on low flows in North America. Hydrological Sciences Journal, 66(4), 689–702, 2021.

Damour, G., Simonneau, T., Cochard, H. and Urban, L.: An overview of models of stomatal conductance at the leaf level. Plant, Cell and Environment, 33(9), 1419–1438, 2010.

Douglas, E. M., Jacobs, J. M., Sumner, D. M. and Ray, R. L.: A comparison of models for estimating potential evapotranspiration for Florida land cover types. Journal of Hydrology, 373, 366–376, 2009.

610   Eckhardt, K. and Ulbrich, U.: Potential impacts of climate change on groundwater recharge and streamflow in a central European low mountain range. Journal of Hydrology, 284(1−4), 244−252, 2003.

ECMWF: IFS   Documentation-Cy31r1   Part   IV: Physical   Processes. http://www.ecmwf.int/sites/default/files/elibrary/2007/9221-part-iv-physical-processes.pdf, 2007.

Elfarkh, J., Er-Raki, S., Ezzahar, J., Chehbouni, A., Aithssaine, B., Amazirh, A., Khabba, S. and Jarlan, L.: Integrating thermal
615   stress indexes within Shuttleworth-Wallace model for evapotranspiration mapping over a complex surface. Irrigation Science, 39, 45–61, 2021.

Espadafor, M., Lorite, I. J., Gavilán, P. and Berengena, J.: An analysis of the tendency of reference evapotranspiration estimates and other climate variables during the last 45 years in Southern Spain. Agricultural Water Management, 98, 1045–1061, 2011.

Fang,H., Jiang,C., Li, W., Wei, S., Baret, F., Chen, J. M., Garcia-Haro, J., Liang, S., Liu, R., Myneni, R. B., Pinty, B.,
620   Xiao, Z. and Zhu, Z.: Characterization and intercomparison of Global Moderate Resolution Leaf Area Index (LAI) products:

Analysis of climatologies and theoretical uncertainties. Journal of Geophysical Research: Biospheres, 118(2), 529–548, 2013.

Field, C. B., Jackson, R. B. and Mooney, H. A.: Stomatal responses to increased CO_2: implications from the plant to the global scale. Plant, Cell & Environment, 18(10), 1214−1225, 1995.

Fisher, J. B., DeBiase, T. A., Qi, Y., Xu, M. and Goldstein, A. H.: Evapotranspiration models compared on a Sierra Nevada
625 forest ecosystem. Environmental Modelling & Software, 20, 783–796, 2005.

Fisher, J. B., Whittaker, R. J. and Malhi, Y.: ET come home: potential evapotranspiration in geographical ecology. Global Ecology and Biogeography, 20, 1–18, 2011.

Foken, T.: The energy balance closure problem: an overview. Ecological Applications, 18(6), 1351–1367, 2008.

Franks, P. J. and Beerling, D. J.: Maximum leaf conductance driven by CO_2 effects on stomatal size and density over geologic
630 time. Proceedings of the National Academy of Sciences, 106(25), 10343–10347, 2008.

Friedl, M. A., Sulla-Menashe, D., Tan, B., Schneider, A., Ramankutty, N., Sibley, A. and Huang, X.: MODIS Collection 5 global land cover: algorithm refinements and characterization of new datasets. Remote Sensing of Environment, 114(1), 68–182, 2010.

Gang, C. –C, Wang, Z. –Q, Yang, Y., Chen, Y. –Z., Zhang, Y. –Z., Li, J. –L. and Cheng, J. –M.: The NPP spatiotemporal
635 variation of global grassland ecosystems in response to climate change over the past 100 years. Acta Prataculturae Sinica, 25(11), 1–14, 2016. (in Chinese with English Abstract)

Gardiol, J. M., Serio, L. A. and Maggiora, A. I. D.: Modeling evapotranspiration of corn (Zea mays) under different plant densities. Journal of Hydrology, 217, 188–196, 2003.

Gardner, A., Jiang, M., Ellsworth, D., MacKenzie, A. R., Pritchard, J., Bader, M. K. –F., Barton, C., Bernacchi, C., Calfapietra,
640 C., Crous, K. Y., Dusenge, M. E., Gimeno, T. E., Hall, M., Lamba, S., Leuzinger, S., Uddling, J., Warren, J., Wallin, G. and Medlyn, B.: Optimal stomatal theory predicts CO_2 responses of stomatal conductance in both gymnosperm and angiosperm trees. New Phytologist, 153, 477–484, 2022.

Gash, J. H. C., Lloyd, C. R. and Lachaud, G.: Estimating sparse forest rainfall interception with an analytical model. Journal of Hydrology, 170(1–4), 79–86, 1995.

645 Gedney, N., Cox, P. M., Betts, R. A., Boucher, O., Huntingford, C. and Stott, P. A.: Detection of a direct carbon dioxide effect in continental river runoff records. Nature, 439(7078), 835–838, 2006.

Gentine, P., Entekhabi, D. and Polcher, J.: The diurnal behavior of evaporative fraction in the soil-vegetation-atmospheric boundary layer continuum, Journal of Hydrometeorology, 12, 1530–1546, 2011.

Gentine, P., Entekhabi, D., Chehbouni, A., Boulet, G. and Duchemin, B.: Analysis of evaporative fraction diurnal behavior.
650 Agricultural and Forest Meteorology, 143, 13–29, 2007.

Gong, X., Liu, H., Sun, J., Gao, Y., Zhang, X., Jha, S. K., Zhang, H., Ma, X. and Wang, W.: A proposed surface resistance

model for the Penman-Monteith formula to estimate evapotranspiration in a solar greenhouse. Journal of Arid Land, 9, 530–546, 2017.

Gupta, H. V., Kling, H., Yilmaz, K. K., Martinez, G. F.: Decomposition of the mean squared error and NSE performance criteria: Implications for improving hydrological modelling. Journal of Hydrology, 377, 80–91, 2012.

Hargreaves, G. H. and Samani, Z. A.: Estimating potential evapotranspiration. Journal of the Irrigation and Drainage Division, Proceedings of the American Society of Civils Engineers, 108, 225–230, 1983.

Harris, I., Osborn, T. J., Jones, P. and Lister, D.: Version 4 of the CRU TS monthly high-resolution gridded multivariate climate dataset. Scientific Data, 7, 109, https://doi.org/10.1038/s41597-020-0453-3, 2020.

Hersbach, H., Bell, B., Berrisford, P., Hirahara, S., Horányi, A., Muñoz-Sabater, J., Nicolas, J., Peubey, C., Radu, R., Schepers, D., Simmons, A., Soci, C., Abdalla, S., Abellan, X., Balsamo, G., Bechtold, P., Biavati, G., Bidlot, J., Bonavita, M., De Chiara, G., Dahlgren, P., Dee, D., Diamantakis, M., Dragani, R., Flemming, J., Forbes, R., Fuentes, M., Geer, A., Haimberger, L., Healy, S., Hogan, R. J., Hólm, E., Janisková, , M., Keeley, S., Laloyaux, P., Lopez, P., Lupu, C., Radnoti, G., Rosnay, P., Rozum, I., Vamborg, F., Villaume, S. and Thépaut, J. –N.: The ERA5 global reanalysis. Quarterly Journal of the Royal Meteorological Society, 146, 1999–2049, 2020.

Hawkins, B.A, Field, R., Cornell, H.V., Currie, D.J., Guégan, J.F., Kaufman, D.M., Kerr, J.T., Mittelbach, G.G., Oberdorff, T., and O'Brien, E.M.: Energy, water, and broad-scale geographic patterns of species richness. Ecology, 84(12), 3105–3117, 2003.

Hinkelman, L. M.: The Global Radiative Energy Budget in MERRA and MERRA-2: Evaluation with Respect to CERES EBAF Data. Journal of Climate, 32, 1973–1994, 2019.

Hu, Z., Li, S., Yu, G., Sun, X., Zhang, L. and Han, S.: Modeling evapotranspiration by combing a two-source model, a leaf stomatal model, and a light-use efficiency model. Journal of Hydrology, 501, 186–192, 2013.

Hu, Z., Yu, G., Zhou, Y., Sun, X., Li, Y. and Shi, P.: Partitioning of evapotranspiration and its controls in four grassland ecosystems: application of a two-source model. Agricultural and Forest Meteorology, 149(9), 1410–1420, 2009.

Hu, Z., Yu, G., Zhou, Y., Sun, X., Li, Y., Shi, P., Wang, Y., Song, X., Zheng, Z., Zhang, L. and Li, S.: Partitioning of evapotranspiration and its controls in four grassland ecosystems: Application of a two-source model. Agricultural and Forest Meteorology, 149(9), 1410–1420, 2009.

Huang, H., Liu, C., Wang, X., Biging, G. S., Chen, Y., Yang, J. and Gong, P.: Mapping vegetation heights in China using slope correction ICESat data, SRTM, MODIS-derived and climate data. ISPRS Journal of Photogrammetry and Remote Sensing, 129, 189–199, 2017.

Huang, S., Yan, H., Zhang, C., Wang, G., Acquah, S. J., Yu, J., Li, L., Ma, J. and Darko, R. O.: Modeling evapotranspiration for cucumber plants based on the Shuttleworth-Wallace model in a Venlo-type greenhouse. Agricultural Water Management, 228, 105861, https://doi.org/10.1016/j.agwat.2019.105861, 2020.

International Food Policy Research Institute: Global spatially-disaggregated crop production statistics data for 2010 version 2.0. Harvard Dataverse [dataset], https://doi.org/10.7910/DVN/PRFF8V, 2019.

685 IPCC: Summary for policymakers. In: Field, C. B., Barros, V. R., Dokken, D. J., Mach, K. J., Mastrandrea, M. D., Bilir, T. E., Chatterjee, M., Ebi, K. L., Estrada, Y. O., Genova, R. C., Girma, B., Kissel, E. S., Levy, A. N., MacCracken, S., Mastrandrea, P. R., White, L. L. (eds.). Climate change 2014: impacts, adaptation, and vulnerability. part a: global and sectoral aspects. contribution of working group ii to the fifth assessment report of the intergovernmental panel on climate change. Cambridge University Press, Cambridge, pp. 1–32, 2014.

690 Iritz, Z., Lindroth, A., Heikinheimo, M., Grelle, A. and Kellner, E.: Test of a modified Shuttleworth-Wallace estimate of boreal forest evaporation. Agricultural and Forest Meteorology, 98–99, 605–619, 1999.

Itenfisu, D., Elliot, R., Allen, R. and Walter, I.: Comparison of reference evapotranspiration calculations across a range of climates, in: Proceedings of the 4th National Irrigation Symposium, St. Joseph, ASAE Edn., 216–227, 2000.

Jarvis, P. G.: Interpretation of variations in leaf water potential and stomatal conductance found in canopies in field.

695 Philosophical Transactions of the Royal Society B Biological Sciences, 273(927), 593–610, 1976.

Jensen, M., Burman, R. and Allen, R.: Evapotranspiration and irrigation water requirements, in: ASCE manual No. 70, p. 332, New York, ASCE Edn., 1990.

Jourdier, B.: Evaluation of ERA5, MERRA-2, COSMO-REA6, NEWA and AROME to simulate wind power production over France. Advances in Science and Research, 17, 63–77, 2020.

700 Kadeba, A., Nacoulma, B. M. I., Ouédraogo, A., Bachmann, Y., Thiombiano, A., Schmidt, M. and Boussim, J. I.: Land cover change and plants diversity in the Sahel: a case study from northern Burkina Faso. Annals of Forest Research, 58(1), 109–123, 2015.

Kerr, J.: 2001. Butterfly species richness patterns in Canada: energy, heterogeneity, and the potential consequences of climate change. Conservation Ecology, 5(1), https://doi.org/10.5751/ES-00246-050110, 2001.

705 Kool, D., Agam, N., Lazarovitch, N., Heitman, J. L., Sauer, T. J. and Ben-Gal, A.: A review of approaches for evapotranspiration partitioning. Agricultural and Forest Meteorology, 184, 56–70, 2014.

Lagos, L. O., Martin, D. L., Verma, S. B., Irmak, S., Irmak, A., Eisenhauer, D. and Suyker, A.: Surface energy balance model of transpiration from variable canopy cover and evaporation from residue-covered or bare soil systems: model evaluation. Irrigation Science, 31(2), 135–150, 2013.

710 Lang, N., Kalischek, N., Armston, J., Schindler, K., Dubayah, R. and Wegner, J. D.: Global canopy height regression and uncertainty estimation from GEDI LIDAR waveforms with deep ensembles. Remote Sensing of Environment, 268, 112760, https://doi.org/10.1016/j.rse.2021.112760, 2022.

Lang, N., Kalischek, N., Armston, J., Schindler, K., Dubayah, R., and Wegner, J. D.: Global canopy top height estimates from

GEDI LIDAR waveforms for 2019. Zenodo [dataset], https://doi.org/10.5281/zenodo.5112903, 2021.

715   Lawrence, D. M., Thornton, P. E., Oleson, K. W. and Bonan, G. B.: The partitioning of evapotranspiration into transpiration, soil evaporation, and canopy evaporation in a GCM: impacts on land-atmosphere interaction. Journal of Hydrometeorology, 8(4), 862–880, 2007.

Lhomme, J. P.: Stomatal control of transpiration: Examination of the Jarvis-type representation of canopy resistance in relation to humidity. Water Resources Research, 37(3), 689–699, 2001.

720   Li, H. and Ma, Y.: Application on classification of Qinghai grassland by advanced comprehensive and sequential classification. Acta Prataculturae Sinica, 18(2), 76–82, 2009. (in Chinese with English Abstract)

Liang, S., Zhao, X., Liu, S., Yuan, W., Cheng, X., Xiao, Z., Zhang, X., Liu, Q., Cheng, J., Tang, H., Qu, Y., Bo, Y., Qu, Y., Ren, H., Yu, K. and Twonshend, J.: A long-term Global LAnd Surface Satellite (GLASS) data-set for environmental studies. International Journal of Digital Earth, 6, 5–33, 2013.

725   Liang, T. G., Feng, Q. S., Huang, X. D. and Ren, J. D.: Review in the study of comprehensive sequential classification system of grassland. Acta Prataculturae Sinica, 20(5), 252–258, 2011. (in Chinese with English Abstract)

Lin, Y. –S., Medlyn, B. E., Duursma, R. A., Prentice, I. C., Wang, H., Baig, S., Eamus, D., de Dios, V. R., Mitchell, P., Ellsworth, D. S., de Beeck, M. O., Wallin, G., Uddling, J., Tarvainen, L., Linderson, M. –L., Cernusak, L. A., Nippert, J. B., Ocheltree, T. W., Tissue, D. T., Martin-StPaul, N. K., Rogers, A., Warren, J. M., De Angelis, P., Hikosaka, K., Han, Q., Onoda, Y., Gimeno,

730   T. E., Barton, C. V. M., Bennie, J., Bonal, D., Bosc, A., Löw, M., Macinins-Ng, C., Rey, A., Rowland, L., Setterfield, S. A., Tausz-Posch, S., Zaragoza-Castells, J., Broadmeadow, M. S. J., Drake, J. E., Freeman, M., Ghannoum, O., Hutley, L. B., Kelly, J. W., Kikuzawa, K., Kolari, P., Koyama, K., Limousin, J. –M., Meir, P., da Costa, A. C. L., Mikkelsen, T. N., Salinas, N., Sun, W., and Wingate, L.: Optimal stomatal behaviour around the world. Nature Climate Change, 5, 459–464, 2015.

Liu, C., Sun G., McNulty, S. G. and Kang, S.: An improved evapotranspiration model for an apple orchard in northwestern

735   China. Transactions of the American Society of Agricultural and Biological Engineers, 58(5), 1253–1264, 2015.

Liu, C., Sun, G., McNulty, S.G., Noormets, A. and Fang, Y.: Environmental controls on seasonal ecosystem evapotranspiration/potential evapotranspiration ratio as determined by the global eddy flux measurements. Hydrology and Earth System Sciences, 21(1), 311–322, 2017.

Liu, H., Gong, P., Wang, J., Nicholas, C., Bai, Y., Liang, S.: Annual dynamics of global land cover and its long-term changes

740   from 1982 to 2015. Earth System Science Data, 12(2), 1217–1243, 2020a.

Liu, H., Gong, P., Wang, J., Nicholas, C., Bai, Y., Liang, S.: Annual dynamics of global land cover and its long-term changes from 1982 to 2015. PANGAEA [dataset], https://doi.org/10.1594/PANGAEA.913496, 2020b.

Liu, J., Chen, J. M. and Cihlar, J.: Mapping evapotranspiration based on remote sensing: an application to Canada's landmass. Water Resources Research, 39(7), https://doi.org/10.1029/2002WR001680, 2003.

745   Liu, X., Xu, C., Zhong, X., Li, Y., Yuan, X. and Cao, J.: Comparison of 16 models for reference crop evapotranspiration against weighing lysimeter measurement. Agricultural Water Management, 184, 145–155, 2017.

Liu, Y., Liu, R. and Chen, J. M.: Retrospective retrieval of long-term consistent global leaf area index (1981–2011) from combined AVHRR and MODIS data. Journal of Geophysical Research: Biogeosciences, 117, G04003, doi:10.1029/2012JG002084, 2012.

750   Liu, Y., Xiao, J., Ju, W., Zhu, G., Wu, X., Fan, W., Li, D. and Zhou, Y.: Satellite-derived LAI products exhibit large discrepancies and can lead to substantial uncertainty in simulated carbon and water fluxes. Remote Sensing of Environment, 206, 174–188, 2018.

Lo Seen, D., Chehbouni, A., Njoku, E., Saatchi, S., Mougin, E. and Monteny, B.: An approach to couple vegetation functioning and soil-vegetation-atmosphere-transfer models for semiarid grasslands during the HAPEX-Sahel experiment. Agricultural

755   and Forest Meteorology, 83(1–2), 49–74, 1997.

Lu, J., Sun, G., McNulty, S. G. and Amatya, D. M.: A comparison of six potential evapotranspiration methods for regional use in the southeastern United States. Journal of the American Water Resources Association, 41(3), 621–633, 2005.

Lu, J., Sun, G., McNulty, S. G. and Amatya, D. M.: Modeling actual evapotranspiration from forested watersheds across the southeastern United States. Journal of the American Water Resources Association, 39(4), 886–896, 2003.

760   Maes, W. H., Gentine, P., Verhost, N. E. C. and Miralles, D.: Potential evaporation at eddy-covariance sites across the globe. Hydrology and Earth System Sciences, 23, 925–948, 2019.

Maes, W. H., Pashuysen, T., Trabucco, A., Veroustraete, F. and Muys, B.: Does energy dissipation increase with ecosystem succession? Testing the ecosystem exergy theory combining theoretical simulations and thermal remote sensing observations. Ecological Modelling, 23–24, 3917–3941, 2011.

765   Martens, B., Miralles, D. G., Lievens, H., van der Schalie, R., de Jeu, R. A. M., Fernández-Prieto, D., Beck, H. E., Dorigo, W. A. and Verhoest, N. E. C.: GLEAM v3: satellite-based land evaporation and root-zone soil moisture. Geoscientific Model Development, 10, 1903–1925, 2017.

Martínez-Vilalta, J., Poyatos, R., Aguadé, D., Retana, J. and Mencuccini, M.: A new look at water transport regulation in plants. New Phytologist, 204, 105–115, 2014.

770   McVicar, T. R., Van Niel, T. G., Li, L. T., Hutchinson, M. F., Mu, X. M. and Liu, Z. H.: Spatially distributing monthly reference evapotranspiration and pan evaporation considering topographic influences, Journal of Hydrology, 338, 196–220, 2007

Medlyn, B. E., Barton, C. V. M., Broadmeadow, M. S. J., Ceulemans, R., De Angelis, P., Forstreuter, M., Freeman, M., Jackson, S. B., Kellomäki, S., Laitat, E., Rey, A., Roberntz, P., Sigurdsson, B. D., Strassemeyer, J., Wang, K., Curtis, P. S. and Jarvis, P. G.: Stomatal conductance of forest species after long-term exposure to elevated CO_2 concentrations: a synthesis. New

775   Phytologist, 149, 247–264, 2001.

Milly, P. C. and Dunne, K. A.: Potential evapotranspiration and continental drying. Nature Climate Change, 6, 946–951, 2016.

Miralles, D. G., Holmes, T. R. H., de Jeu, R. A. M., Gash, J. H., Meesters, A. G. C. A. and Dolman, A. J.: Global land-surface evaporation estimated from satellite-based observations. Hydrology and Earth System Sciences, 15, 453–469, 2011.

Mizutani, K., Yamanoi, K., Ikeda, T. and Watanabe, T.: Applicability of the eddy correlation method to measure sensible heat
780 transfer to forest under rainfall conditions. Agricultural and Forest Meteorology, 86, 193–203, 1997.

Mo, X., Liu, S., Lin, Z. and Zhao, W.: Simulating temporal and spatial variation of evapotranspiration over the Lushi basin. Journal of Hydrology, 285, 125–142, 2004.

Molod, A., Takacs, L., Suarez, M. and Bacmeister, J.: Development of the GEOS-5 atmospheric general circulation model: Evolution from MERRA to MERRA-2. Geoscientific Model Development, 8, 1339–1356, 2015.

785 Monteith, J. L.: Evaporation and environment, Symposia of the society for experimental biology, Cambridge University Press, Cambridge, 1965.

Morison, J. I. L. and Gifford, R. M.: Plant growth and water use with limited water supply in high CO_2 concentrations. I. Leaf area, water use and transpiration. Functional Plant Biology, 11(5), 361−374, 1984.

Mu, Q. Z., Zhao, M. S. and Running, S.W.: Improvements to a MODIS global terrestrial evapotranspiration algorithm. Remote
790 Sensing of Environment, 115(8), 1781–1800, 2011.

Mu, Q., Zhao, M. and Running, S. W.: MODIS Global Terrestrial Evapotranspiration (ET), Product (NASA MOD16A2/A3), Algorithm Theoretical Basis Document, Collection 5, NASA Headquarters, 2013.

Neitsch, S. L., Arnold, J. G., Kiniry, J. R., Williams, J. R. and King, K. W.: Soil and Water Assessment Tool Theoretical Documentation, Version 2000. Soil and Water Research Laboratory and Blackland Research Center, Grassland, 2002.

795 Noilhan, J. and Planton, S.: A simple parameterization of land surface processes for meteorological models. Monthly Weather Review, 117: 536–549, 1989.

Norby, R. J., Delucia, E. H., Gielen, B., Calfapietra, C., Giardina, C. P., King, J. S., Ledford, J., McCarthy, H. R., Moore, D. J., Ceulemans, R., De Angelis, P., Finzi, A. C., Karnosky, D. F., Kubiske, M. E., Lukac, M., Pregitzer, K. S., Scarascia-Mugnozza, G. E., Schlesinger, W. H. and Oren, R.: Forest response to elevated CO_2 is conserved across a broad range of
800 productivity. Proceedings of the National Academy of Sciences, 102(50), 18052–18056, 2005.

Nutini, F., Boschetti, M., Candiani, G., Bocchi, S. and Brivio, P. A.: Evaporative fraction as an indicator of moisture condition and water stress status in semi-arid rangeland ecosystems. Remote Sensing, 6, 6300–6323, 2014.

Odhiambo, L. O. and Irmak, S.: Performance of extended Shuttleworth-Wallace model for estimating and partitioning of evapotranspiration in a partial residue-covered subsurface drip-irrigated soybean field. Transactions of the American Society
805 of Agricultural and Biological Engineers, 54(3), 915-930, 2011.

Pastorello, G., Trotta, C., Canfora, E., Chu, H., … and Papale, D.: The FLUXNET2015 dataset and the ONEFlux processing

pipeline for eddy covariance data. Scientific Data, 7, 225, https://doi.org/10.1038/s41597-020-0534-3, 2020.

Penman, H. L.: Natural evaporation from open water, bare soil and grass. Proceedings of the Royal Society of London. Series A: Mathematical and physical sciences, 1032, 120–145, 1948.

810 Pereira, L. S., Perrier, A., Allen, R. G. and Alves, I.: Evapotranspiration: Concepts and future trends. Journal of Irrigation and Drainage Engineering, 125, 45–51, 1999.

Phillips, L.B, Hansen, A.J., Flather, C.H., and Robison-Cox, J.: Applying species-energy theory to conservation: a case study for North American birds. Ecological Applications, 20(7), 2007–2023, 2010.

Piao, S. L., Friedlingstein, P., Ciais, P., de Noblet-Ducoudré, N., Labat, D. and Zaehle, S.: Changes in climate and land use

815 have a larger direct impact than rising CO_2 on global river runoff trends. Proceedings of the National Academy of Sciences, 104(39), 5242–15247, 2007.

Potapov, P., Li, X., Hernandez-Serna, A., Tyukavina, A., Hansen, M. C., Kommareddy, A., Pickens, A., Turubanova, S., Tang, H., Silva, C. E., Armston, J., Dubayah, R., Blair, J. B. and Hofton, M.: Mapping and monitoring global forest canopy height through integration of GEDI and Landsat data. Remote Sensing of Environment, 112165,

820 https://doi.org/10.1016/j.rse.2020.112165, 2020.

Powell, T. L., Bracho, R., Li, J., Dore, S., Hinkle, C. R. and Drake, B. G.: Environmental controls over net ecosystem carbon exchange of scrub oak in central Florida. Agricultural and Forest Meteorology, 141, 19–34, 2006.

Prakash, V., Bera, T., Pradhan, S. and Acharya, S. K.: Potential of Syngonanthus nitens fiber as a reinforcement in epoxy composite and its mechanical characterization. Journal of the Indian Academy of Wood Science, 17, 73–81, 2020.

825 Raab, N., Meza, F. J., Frank, N. and Bambach, N.: Empirical stomatal conductance models reveal that the isohydric behavior of an Acacia caven Mediterranean Savannah scales from leaf to ecosystem. Agricultural and Forest Meteorology, 213, 203–216, 2015.

Rao, L. Y., Sun, G., Ford, C. R. and Vose, J. M.: Modeling potential evapotranspiration of two forested watersheds in the southern Appalachians. Transactions of the ASABE, 54(6), 2067–2078, 2011.

830 Reddy, S. J.: An empirical method for estimating sunshine from total cloud amount. Solar Energy, 15(4), 281–285, 1974.

Roderick, M. L., Greve, P. and Farquhar G. D.: On the assessment of aridity with changes in atmospheric CO_2. Water Resources Research, 51, 5450–5463, 2015.

Running, S., Mu, Q. and Zhao, M.: MOD16A2 MODIS/Terra Net Evapotranspiration 8-Day L4 Global 500m SIN Grid V006. 2017.

835 Saxe, H., Ellsworth, D. and Heath, J.: Tree and forest functioning in an enriched CO_2 atmosphere. New Phytologist, 139(3), 395−436, 1998.

Scheff, J.: Drought indices, drought impacts, CO_2, and warming: A historical and geologic perspective. Current Climate

Change Reports, 4, 202−209, 2018.

Seiller, G. and Anctil, F.: How do potential evapotranspiration formulas influence hydrological projections? Hydrological
840   Sciences Journal, 61(12), 2249–2266, 2016.

Sheffield, J., Wood, E. F. and Roderick, M. L.: Little change in global drought over the past 60 years. Nature, 491(7424), 435–
438, 2012.

Shuttleworth, W. J. and Wallace, J. S.: Evaporation from sparse crops—an energy combination theory. Quarterly Journal of
the Royal Meteorological Society, 111, 839–855, 1985.

845   Shuttleworth, W. J. and Wallace, J. S.: Evaporation from sparse crops: An energy combination theory. Quarterly Journal of the
Royal Meteorological Society, 111(469), 839–855, 1985.

Simard, M., Pinto, N., Fisher, J. B. and Baccini, A.: Mapping forest canopy height globally with spaceborne lidar. Journal of
Geophysical Research: Space Physics, 116, G0402, https://doi.org/10.1029/2011JG001708, 2011.

Singer, M. B., Asfaw, D. T., Rosolem, R., Cuthbert, M. O., Miralles, D. G., MacLeod, D., Quichimbo, E. A. and Michaelides,
850   K.: Hourly potential evapotranspiration at 0.1° resolution for the global land surface from 1981–present. Scientific Data, 8,
224, https://doi.org/10.1038/s41597-021-01003-9, 2021.

Singh, V. P. and Xu, C. –Y.: Evaluation and generalization of 13 equations for determining free water evaporation. Hydrological
Processes, 11, 311–323, 1997.

Stannard, D. I.: Comparison of Penman-Monteith, Shuttleworth-Wallace, and modified Priestley-Taylor evapotranspiration
855   models for wildland vegetation in semiarid rangeland. Water Resources Research, 29(5), 1379–139, 1993.

Sun, G., Alstad, K., Chen, J., Ford, C. R., Lin, G., Liu, C., Nan, L., McNulty, S. G. and Miao, H.: A general predictive model
for estimating monthly ecosystem evapotranspiration. Ecohydrology, 4(2), 245–255, 2011a.

Sun, G., Caldwell, P., Noormets, A., McNulty, S. G., Cohen, E., Myers, J. M., Domec, J. –C., Treasure, E., Mu, Q., Xiao, J.,
John, R. and Chen, J.: Upscaling key ecosystem functions across the conterminous United States by a water-centric ecosystem
860   model. Journal of Geophysical Research: Biogeosciences, 116(G3), G00J05, https://doi.org/10.1029/2010JG001573, 2011b.

Sun, S., Bi, Z., and Chen, H.: A global 5 km monthly potential evapotranspiration dataset (1982–2015) estimated by the
Shuttleworth-Wallace   model.   National   Tibetan   Plateau/Third   Pole   Environment   Data   Center,
https://doi.org/10.11888/Terre.tpdc.300193. https://cstr.cn/18406.11.Terre.tpdc.300193, 2023.

Sun, S., Bi, Z., Zhou, S., Wang, H., Li, Q., Liu, Y., Wang, G., Li, S., Chen, H. and Zhou, Y.: Spatiotemporal shifts in key
865   hydrological   variables   and   dominant   factors   over   China.   Hydrological   Processes,   35,   e14319,
https://doi.org/10.1002/hyp.14319, 2021.

Sun, S., Chen, H., Ju, W., Yu, M., Hua, W. and Yin, Y.: On the attribution of the changing hydrological cycle in Poyang Lake
Basin, China. Journal of Hydrology, 514, 214–225, 2014.

Sun, S., Liu, Y., Chen, Ju, W., Xu, C. –Y., Liu, Y., Zhou, B., Zhou, Y., Zhou, Y. and Yu, M.: Causes for the increases in both
870   evapotranspiration and water yield over vegetated mainland China during the last two decades. Agricultural and Forest
        Meteorology, 324, 109118, https://doi.org/10.1016/j.agrformet.2022.109118, 2022.

Suttie, J. M., Reynolds, S. G. and Batello, C.: Grasslands of the World. Plant Production and Protection Series No. 34. Rome:
        Food and Agriculture Organization of the United Nations, 2005.

Tabari, H. and Talaee, P. H.: Local calibration of the Hargreaves and Priestley-Taylor equations for estimating reference
875   evapotranspiration in arid and cold climates of Iran based on the Penman-Monteith model. Journal of Hydrologic Engineering,
        16, 837–845, 2011.

Tanguy, M., Prudhomme, C., Smith, K. and Hannaford, J.: Historical gridded reconstruction of potential evapotranspiration
        for the UK. Earth System Science Data, 10, 951–968, 2018.

Tanguy, M., Prudhomme, C., Smith, K. and Hannaford, J.: Historical gridded reconstruction of potential evapotranspiration
880   for the UK. Earth System Science Data, 10, 951–968, 2018.

Thornthwaite, C. W.: An approach toward a rational classification of climate. Geographical Review, 38, 55–94, 1948.

Tomas-Burguera, M., Vicente-Serrano, S. M., Beguería, S., Reig, F., and Latorre, B.: Reference crop evapotranspiration
        database in Spain (1961–2014). Earth Science System Data, 11, 1917–1930, 2019.

Tourula, T. and Heikinheimo, M.: Modelling evapotranspiration from a barley field over the growing season. Agricultural and
885   Forest Meteorology, 91(3–4), 237–250, 1998.

Trajkovic, S.: Hargreaves versus Penman-Monteith. Journal of Irrigation and Drainage Engineering, 133, 38–42, 2007.

Trenberth, K. E., Dai, A., van der Schrier, G., Jones, P. D., Barichivich, J., Briffa, K. R. and Sheffield, J.: Global warming and
        changes in drought. Nature Climate Change, 4, 17–22, 2012.

Turc, L.: Estimation of irrigation water requirements, potential evapotranspiration: a simple climatic formula evolved up to
890   date. Annales Agronomiques, 12, 13–49, 1961.

Urraca, R., Huld, T., Amillo, A. M. G., Martinez-de-Pison, F. J., Kaspar, F. and Sanz-Garcia, A.: Evaluation of global horizontal
        irradiance estimates from ERA5 and COSMO-REA6 reanalyses using ground and satellite-based data. Solar Energy, 164, 339–
        354, 2018.

Vicente-Serrano, S. M., Beguería, S. and López-Moreno, J.: A multiscalar drought index sensitive to global warming: the
895   standardized precipitation evapotranspiration index. Journal of Climate, 23, 1696–1718, 2010.

Vicente-Serrano, S. M., McVicar, T. R., Miralles, D. G., Yang, Y. and Tomas-Burguera, M.: Unraveling the influence of
        atmospheric evaporative demand on drought and its response to climate change. WIREs Climate Change, 11, e632,
        https://doi.org/10.1002/wcc.632, 2020.

Villagarcía, L., Were, A., Garcíac, M. and Domingo, F.: Sensitivity of a clumped model of evapotranspiration to surface

900   resistance parameterisations: Application in a semi-arid environment. Agricultural and Forest Meteorology, 150, 1065–1078, 2010.

Wand, S. J. E., Midgley, G. F., Jones, M. H. and Curtis, P. S.: Responses of wild C_4 and C_3 grass (Poaceae) species to elevated atmospheric CO_2 concentrations: a metaanalytic test of current theories and perceptions. Global Change Biology, 5, 723–741, 1999.

905   Wang, H., Guan, H., Liu, N., Soulsby, C., Tetzlaff, D. and Zhang, X.: Improving the Jarvis-type model with modified temperature and radiation functions for sap flow simulations. Journal of Hydrology, 587, 124981, https://doi.org/10.1016/j.jhydrol.2020.124981, 2020.

Wang, K. C. and Dickinson, R. E.: A review on global terrestrial evapotranspiration: observation, modeling, climatology, and Climatic Variability, Reviews of Geophysics, 50, RG2005, https://doi.org/10.1029/2011RG000373, 2012.

910   Wang, Y., Li, G., Ding, J., Guo, Z., Tang, S., Wang, C., Huang, Q., Liu, R. and Chen, J. M.: A combined GLAS and MODIS estimation of the global distribution of mean forest canopy height. Remote Sensing of Environment, 74, 24–43, 2016.

Wei, G., Zhou, L., Liu, H., Tian, Q., Ding, L. and Ran, X.: Improving evapotranspiration model performance by treating energy imbalance and interaction. Water Resources Research, 56(9), e2020WR027367, https://doi.org/10.1029/2020WR027367, 2020.

Wells, N., Goddard, S. and Hayes, M. J.: A self-calibrating palmer drought severity index. Journal of Climate, 17, 2335–2351,

915   2004.

Wever, L. A., Flanagan, L. B. and Carlson, P. J.: Seasonal and interannual variation in evapotranspiration, energy balance and surface conductance in a northern temperate grassland. Agricultural and Forest Meteorology, 112(1), 31–49, 2002.

White, F.: The vegetation of Africa. Paris: Unesco., 1983

Wild, M.: Global dimming and brightening: A review. Journal of Geophysical Research: Atmospheres, 114, D10,

920   https://doi.org/10.1029/2008JD011470, 2009.

Wilson, K., Goldstein, A., Falge, E., Aubinet, M., Baldocchi, D., Berbigier, P., Bernhofer, C., Ceulemans, R., Dolman, H., Field, C., Grelle, A., Ibrom, A., Law, B. E., Kowalski, A., Meyers, T., Moncrieff, J., Monson, R., Oechel, W., Tenhunen, J., Valentini, R. and Verma, S.: Energy balance closure at FLUXNET sites. Agricultural and Forest Meteorology, 113, 223–243, 2002.

925   Winkel, T., Payne, W. and Renno, J. F.: Ontogeny modifies the effects of water stress on stomatal control, leaf area duration and biomass partitioning of Pennisetum glaucum. New Phytologist, 149(1), 71–82, 2001.

Wu, L., Min, L. L., Shen, Y. J., Zhou, X. X. and Liu, F. G.: Simulation of maize evapotranspiration at different growth stages using revised dual-layered model in arid Northwest China. Chinese Journal of Eco-Agriculture, 25(5), 634−646, 2017. (in Chinese with English Abstract)

930   Xiang, K., Li, Y., Horton, R. and Feng, H.: Similarity and difference of potential evapotranspiration and reference crop

evapotranspiration—A review. Agricultural Water Management, 232, 106043, https://doi.org/10.1016/j.agwat.2020.106043, 2020.

Xiao, Z., Liang, S. and Jiang, B.: Evaluation of four long time-series global leaf area index products. Agricultural and Forest Meteorology, 246, 218–230, 2017.

935 Xiao, Z., Liang, S., Wang, J. and Zhao, X.: Long time series Global Land Surface Satellite (GLASS) Leaf Area Index product derived from MODIS and AVHRR data. IEEE Transactions on Geoscience and Remote Sensing, 54(9), 5301–5318, 2016.

Xiao, Z., Liang, S., Wang, J., Chen, P., Yin, X. and Song, J.: Use of general regression neural networks for generating the GLASS Leaf Area Index product from time-series MODIS surface reflectance. IEEE Transactions on Geoscience and Remote Sensing, 52(1), 209–223, 2014.

940 Xiao, Z., Liang, S., Wang, T. and Liu, Q.: Reconstruction of satellite-retrieved land-surface reflectance based on temporally-continuous vegetation indices. Remote Sensing, 7, 9844–9864, 2015.

Xu, B., Li, J., Park, T., Liu, Q., Zeng, Y., Yin, G., Zhao, J., Fan, W., Yang, L. and Knyazikhin, Y.: An integrated method for validating long-term leaf area index products using global networks of site-based measurements. Remote Sensing of Environment, 209, 134–151, 2018.

945 Xu, B., Li, J., Park, T., Liu, Q., Zeng, Y., Yin, G., Zhao, J., Fan, W., Yang, L., Knyazikhin, Y. and Myneni, R. B.: An integrated method for validating long-term leaf area index products using global networks of site-based measurements. Remote Sensing of Environment, 209, 134–151, 2007.

Xu, C. –Y. and Singh, V. P.: Evaluation and generalization of radiation-based methods for calculating evaporation. Hydrological Processes, 14, 339–349, 2000.

950 Xu, C. –Y. and Singh, V. P.: Evaluation and generalization of temperature-based methods for calculating evaporation. Hydrological Processes, 15, 305–319, 2001.

Yang, Y., Roderick, M. L., Zhang, S., McVicar, T. R. and Donohue, R. J.: Hydrological implications of vegetation responses to elevated CO2 in climate projections. Nature Climate Change, 9, 44–48, 2019.

Yang, Y. and Shang, S.: Comparison of dual-source evapotranspiration models in estimating potential evaporation and
955 transpiration. Transactions of the Chinese Society of Agricultural Engineering, 28(24), 85–91, 2012.

Yin, J., Feng, Q., Liang, T., Meng, B., Yang, S., Gao, J., Ge, J., Hou, M., Liu, J., Wang, W., Yu, H. and Liu, B.: Estimation of grassland height based on the random forest algorithm and remote sensing in the Tibetan Plateau. IEEE Journal of Selected Topics in Applied Earth Observations and Remote Sensing, 13, 178–186, 2019.

Yu, Q., You, L., Wood-Sichra, U., Ru, Y., Joglekar, A. K. B., Fritz, S., Xiong, W., Lu, M., Wu, W. and Peng, Y.: A cultivated
960 planet in 2010—Part 2: The global gridded agricultural-production maps. Earth System Science Data, 12(4), 3545–3572, 2020.

Zhan, C., Orth, R., Migliavacca, M., Zaehle, S., Reichstein, M., Engel, J., Ramming, A. and Winkler, A. J.: Emergence of the

physiological effects of elevated CO_2 on land-atmosphere exchange of carbon and water. Global Change Biology, 28, 7313–7326, 2022.

Zhang, B., Kang, S., Li, F. and Zhang, L.: Comparison of three evapotranspiration models to Bowen ratio-energy balance method for a vineyard in an arid desert region of northwest China. Agricultural and Forest Meteorology, 148(10), 1629−1640, 2008.

Zhang, J., Zhao, T., Li, Z., Li, C., Li, Z., Ying, K., Shi, C., Jiang, L. and Zhang, W.: Evaluation of Surface Relative Humidity in China from the CRA-40 and Current Reanalyses. Advances in Atmospheric Sciences, 38(11), 1958–1976, 2021.

Zhang, Z., Arnault, J., Wagner, S., Laux, P., and Kunstmann, H.: Impact of lateral terrestrial water flow on land-atmosphere interactions in the Heihe River Basin in China: Fully coupled modeling and precipitation recycling analysis. Journal of Geophysical Research: Atmospheres, 124, 8401–8423, 2019.

Zhao, M. and Cao, L.: Regional response of land hydrology and carbon uptake to different amounts of solar radiation modification. Earth's Future, 10, e2022EF003288, https://doi.org/10.1029/2022EF003288, 2022.

Zhao, P., Li, S. E., Li, F. S., Du, T. S., Tong, L. and Kang, S. Z.: Comparison of dual crop coefficient method and Shuttleworth-Wallace model in evapotranspiration partitioning in a vineyard of northwest China. Agricultural Water Management, 160, 41–56, 2015.

Zhou, M. C., Ishidaira, H., Hapuarachchi, H. P., Magome, J., Kiem, A. S. and Takeuchi, K.: Estimating potential evapotranspiration using Shuttleworth-Wallace model and NOAA-AVHRR NDVI data to feed a distributed hydrological model over the Mekong River basin. Journal of Hydrology, 327(1–2), 151–173, 2006.

Zhou, S., Yu, B., Zhang, Y., Huang, Y. and Wang, G.: Partitioning evapotranspiration based on the concept of underlying water use efficiency. Water Resources Research, 52, 1160–1175, 2016.

Zhou, S., Yu, B., Zhang, Y., Huang, Y. and Wang, G.: Water use efficiency and evapotranspiration partitioning for three typical ecosystems in the Heihe River Basin. Agricultural and Forest Meteorology, 253–254, 261–273, 2018.

Zhu, Z., Bi, J., Pan, Y., Ganguly, S., Anav, A., Xu, L., Samanta, A., Piao, S., Nemani, R. R. and Myneni, R. B.: Global data sets of vegetation Leaf Area Index (LAI)3g and Fraction of Photosynthetically Active Radiation (FPAR)3g derived from Global Inventory Modeling and Mapping Studies (GIMMS) Normalized Difference Vegetation Index (NDVI3g) for the period 1981 to 2011. Remote Sensing, 5(2), 927–948, 2013.

Zhu, Z., Piao, S., Myneni, R. B., Huang, M., Zeng, Z., Canadell, J. G., Ciais, P., Sitch, S., Friedlingstein, P., Arneth, A., Cao, C., Cheng, L., Kato, E., Koven, C., Li, Y., Liu, Y., Liu, R., Mao, J., Pan, Y., Peng, S., Peñuelas, J., Poulter, B., Pugh, T. A. M., Stocker, B. D., Viovy, N., Wang, X., Wang, Y., Xioa, Z., Yang, H., Zaehe, S. and Zeng, N.: Greening of the earth and its drivers. Nature Climate Chang, 6(8), 791–795, 2016.
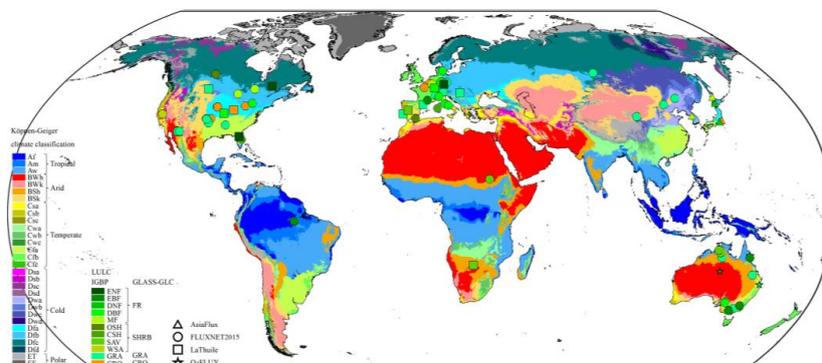
Figure 1: Locations of the used EC sites in this study over Köppen-Geiger (KG) climate regions (Beck et al., 2018). International

995 **Geosphere-Biosphere Programme (IGBP) classification system: CRO—cropland; GRA—grasslands; DBF—deciduous broadleaf**

forest; EBF—evergreen broadleaf forest; ENF—evergreen needleleaf forest; MF—mixed forest; CSH—closed shrubland; WSA—

woody savannah; SAV—savannah; OSH–open shrubland. GLASS-GLC classification system: FR—ENF, EBF, DNF, DBF and MF;

SHRB—SAV CSH, OSH and WSA; GRA; CRO.

1000
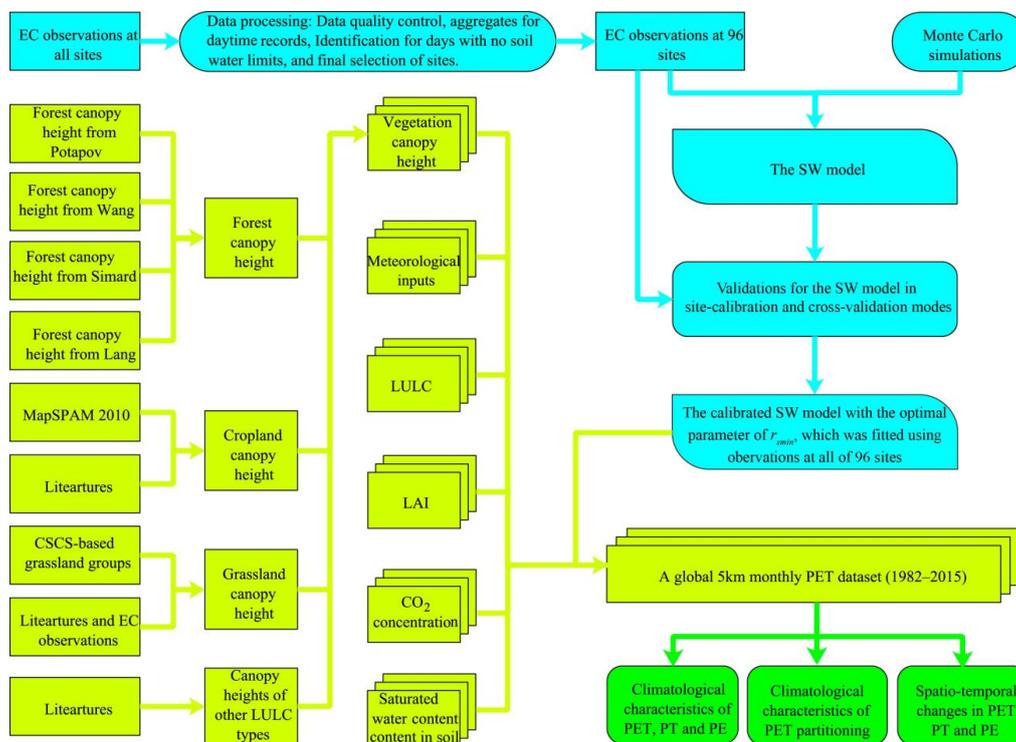
Figure 2: Workflow of this study. The blue and the yellow-green colors show operating procedures for calibrating and validating the SW model and for producing a global 5 km monthly PET dataset, respectively, while the green color presents the related analyses.
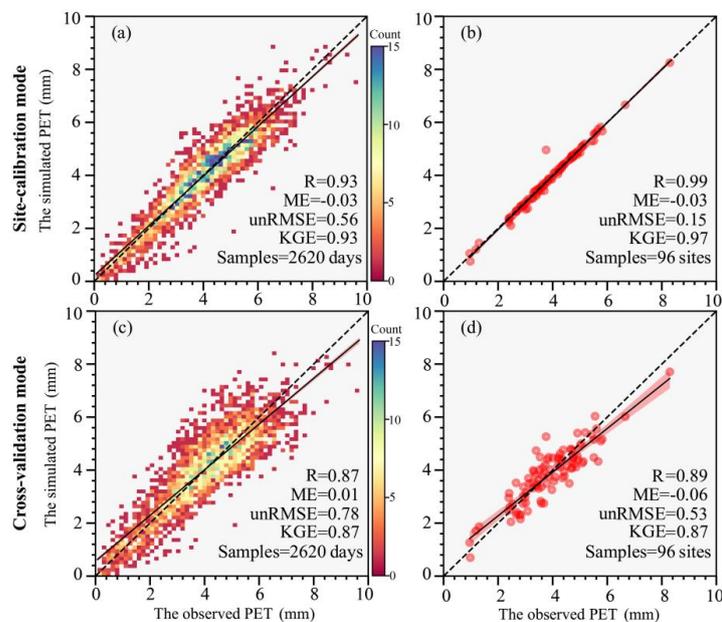
Figure 3: Scatter-plots of observations against simulations aggregated for all of 96 EC sites. (a): Daily comparison in site-calibration mode. (b): Site mean comparison in site-calibration mode. (c): Daily comparison in cross-validation mode. (d): Site mean comparison in cross-validation mode. In these figures, the dash and the solid lines are the 1:1 line and the regression line with the least square method, while the shadow area represents 95% confidence interval.
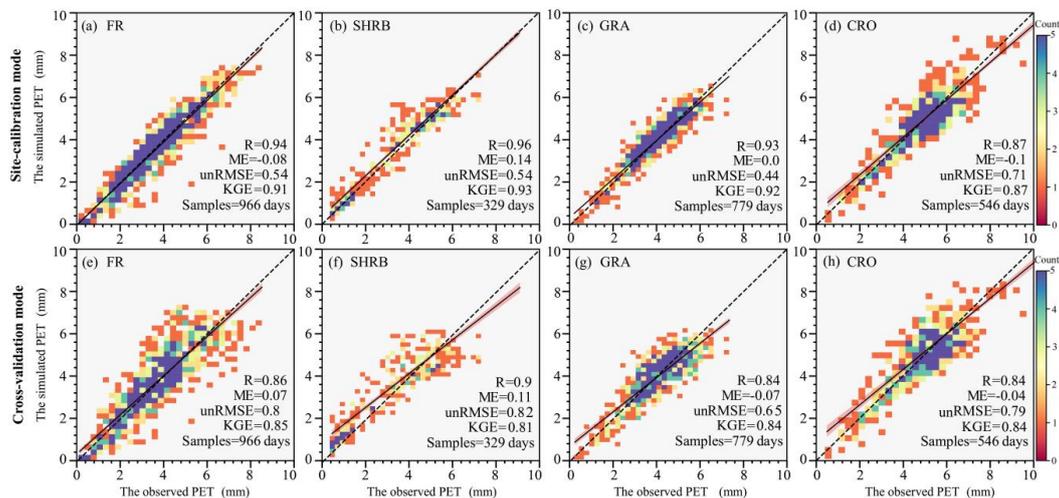
Figure 4: Scatter-plots of daily observations against simulations aggregated for different LULC types. (a–d): Comparison in site-calibration mode. (e–h): Comparison in cross-validation mode. In these figures, the dash and the solid lines are the 1:1 line and the regression line with the least square method, while the shadow area represents 95% confidence interval.
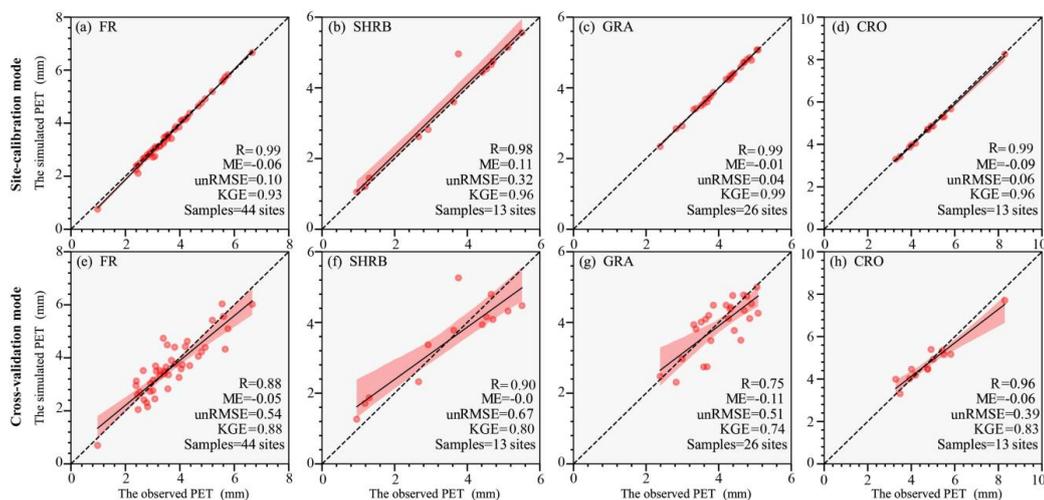
Figure 5: Scatter-plots site mean observations against simulations for each LULC type. (a–d): Comparison in site-calibration mode. (e–h): Comparison in cross-validation mode. In these figures, the dash and the solid lines are the 1:1 line and the regression line with the least square method, while the shadow area represents 95% confidence interval.
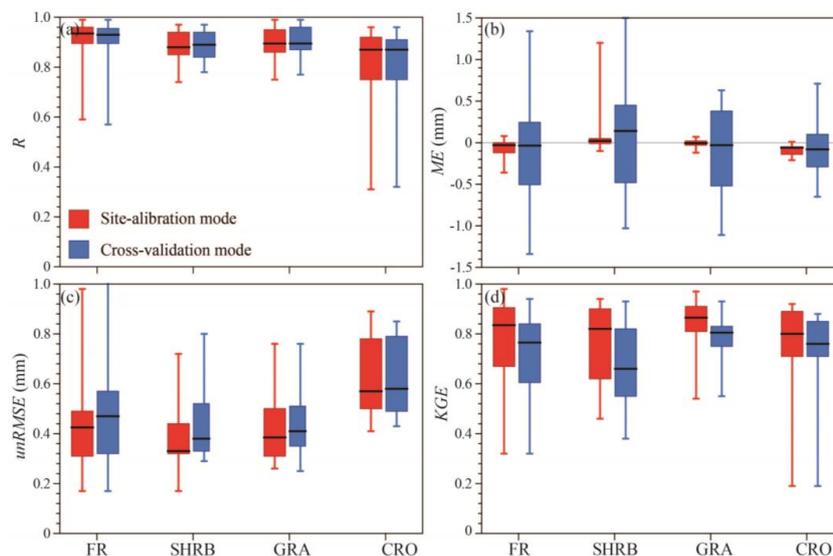
1020

Figure 6: Boxplots of the validation metrics of daily PET simulations for each LULC type. The whiskers represent the minimum and maximum values of the model performance metrics. The outer edges of the boxes and the horizontal lines within the boxes indicate the 25th, 75th, and 50th percentiles of the validation metrics.
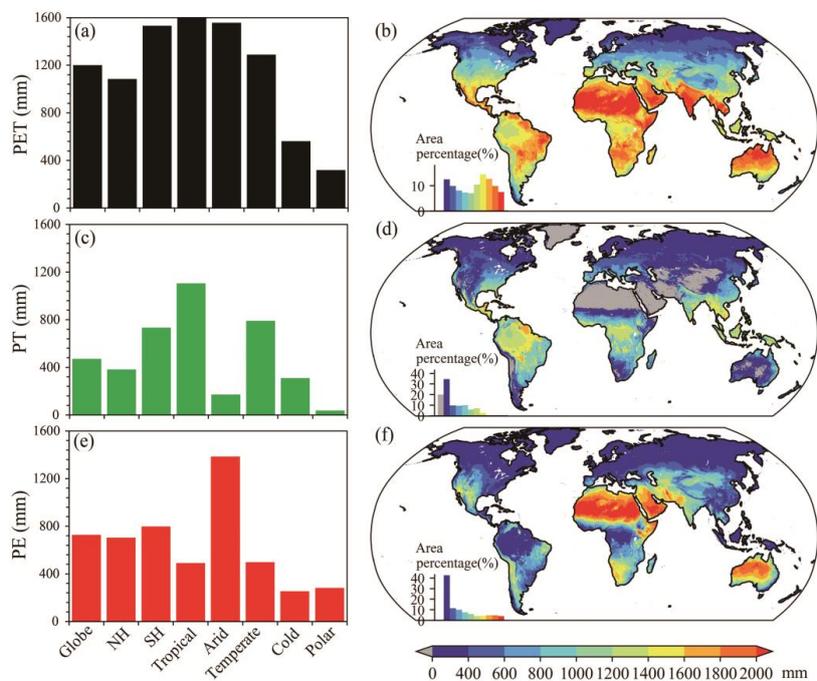
1025

Figure 7. Climatological annual PET, PE and PT. (a): Climatological annual PET averaged over the globe, Northern Hemisphere (NH) and Southern Hemisphere (SH), and each KG climate region. (b): Spatial distribution of climatological annual PET. (c): Climatological annual PT averaged over the globe, NH and SH, and each KG climate region. (d): Spatial distribution of climatological annual PT. (e): Climatological annual PE averaged over the globe, NH and SH, and each KG climate region. (f):

1030 **Spatial distribution of climatological annual PE. In (b), (d) and (f), the inset histogram shows area percentage stratified by the amount of annual PET, PT or PE.**
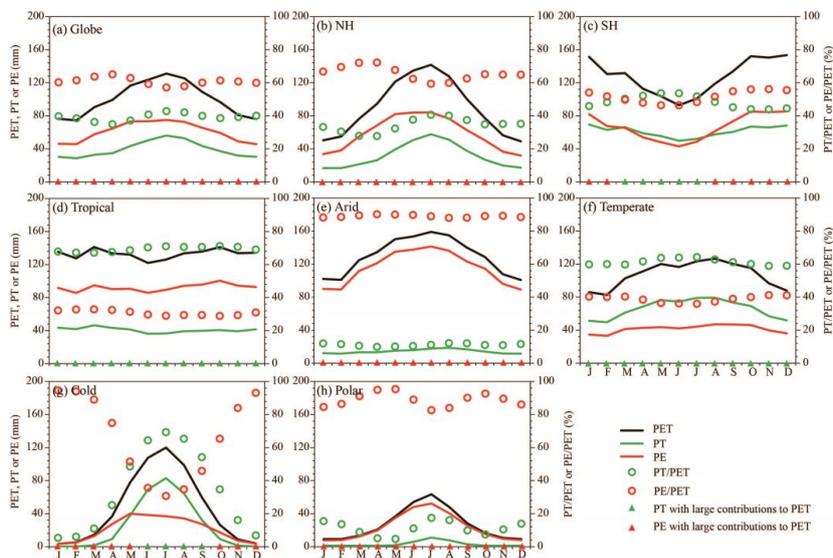
Figure 8: Climatological monthly PET, PE, PT, PE/PET and PT/PET averaged over the globe, each hemisphere, and each KG climate region.
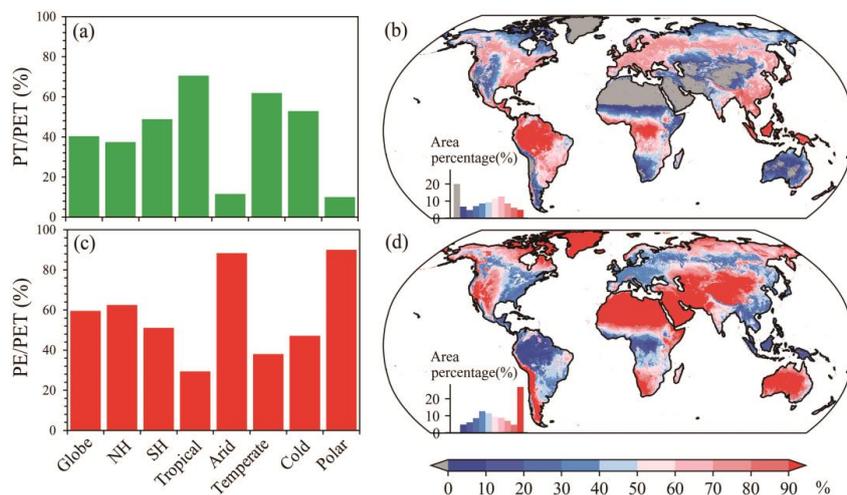
Figure 9: Characteristics of annual PT/PET and PE/PET. (a): Annual PT/PET averaged over the globe, each hemisphere, and each KG climate region. (b): Spatial distribution of annual PT/PET. (c): Annual PE/PET averaged over the globe, each hemisphere, and each KG climate region. (d): Spatial distribution of annual PE/PET. In (b) and (d), the inset histogram shows area percentage stratified by the amount of annual PT/PET or PE/PET.
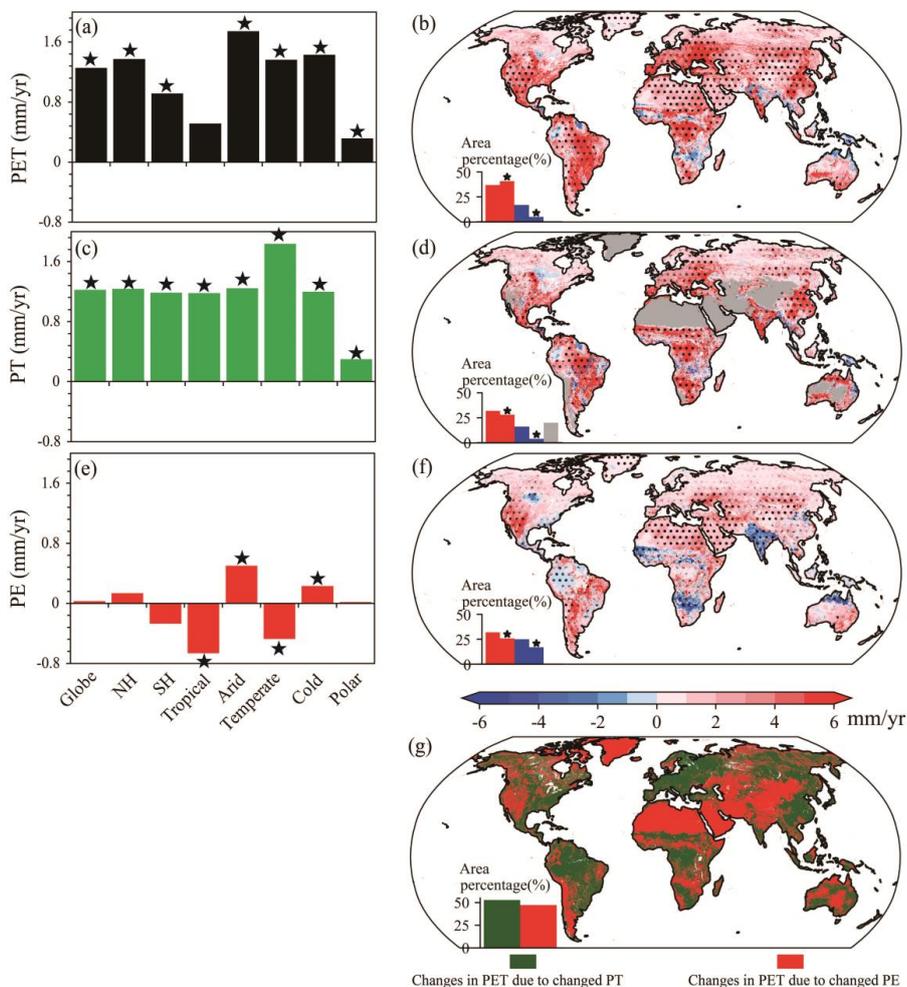
Figure 10: Characteristics of annual PET, PT and PE trends, and major contributors to annual PET trends. (a): Trends for annual PET averaged over the globe, each hemisphere, and each KG climate region. (b): Spatial distribution of annual PET trends. (c): Trends for annual PT averaged over the globe, each hemisphere, and each KG climate region. (d): Spatial distribution of annual PT trends. (e): Trends for annual PE averaged over the globe, each hemisphere, and each KG climate region. (f): Spatial distribution of annual PE trends. (g): Spatial distribution of major contributors to annual PET trends. In (a), (c) and (e), the star indicates that the trend is significant ($p<0.05$). In (b), (d) and (f), the inset histogram suggests area percentage of insignificant increases (red bar without star), significant increases (red bar with star; $p<0.05$), insignificant decreases (blue bar without star), and significant decreases (blue bar with star; $p<0.05$).
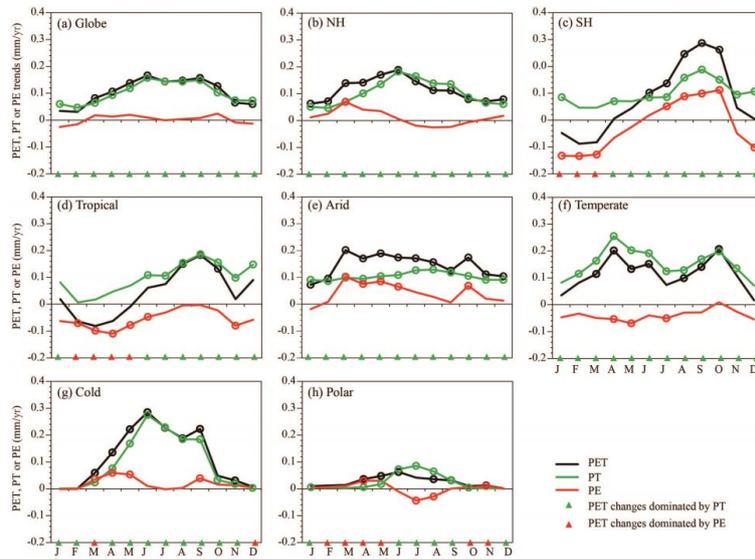
Figure 11: Changes in monthly PET, PT and PE for the globe, each hemisphere, and each KG climate region. The circle indicate that

1055   **the trend is significant with *p*<0.05.**

Table 1: Overview of major inputs for producing the global PET based on the calibrated SW model

Datasets		Basic information		
		Spatio-temporal resolution and time coverage	Variables	Sources and references
Meteorological datasets	MSWX-Past	0.1° × 0.1°; 3-hourly; 1979−present.	Mean, maximum and minimum temperatures, RH, u at 10 m, downward shortwave radiation and downward longwave radiation.	http://www.gloh2o.org/mswx/; Beck et al. (2022)
	CRU TS4.06	0.5° × 0.5°; monthly; 1901−2021.	Mean, maximum and minimum temperatures, cloud cover and ea.	https://crudata.uea.ac.uk/cru/data/hrg/; Harris et al. (2020)
	ERA-5	0.25° × 0.25°; monthly; 1959−present.	Mean, minimuma, maximuma and dewpoint temperatures, surface pressure, u at 10 m, net shortwave radiation and net longwave radiation.	https://cds.climate.copernicus.eu/cdsapp#!/home/; Hersbach et al. (2020) and Berrisford et al. (2021)
	MERRA-2	0.5° × 0.625°; monthly; 1980−present.	Mean, minimuma and maximuma temperatures, specific humidity, surface pressure, u at 10 m wind speed, net shortwave radiation and net longwave radiation.	https://disc.gsfc.nasa.gov/; Molod et al. (2015)
GLASS AVHRR LAI		0.05° × 0.05°; 8-day; 1981−2018.	LAI	http://www.glass.umd.edu/; Xiao et al. (2016, 2017)
GLASS-GLC		5000 m × 5000 m; yearly; 1982−2015.	LULC	https://doi.org/10.1594/PANGAEA.913496; Liu et al. (2020b)
Saturated water content in soil		0.0833° × 0.0833°; static.	Saturated water content in the first soil layer (i.e., 0–0.0451 m)	http://globalchange.bnu.edu.cn/research/soil5.jsp; Dai et al. (2019a, 2019b)
Forest canopy height from Potapov		30 m×30 m; static.	Forest canopy height	https://glad.umd.edu/dataset/gedi/; Potapov et al. (2020)
Forest canopy height from Wang		500 m × 500 m; static.	Forest canopy height	http://www.nsmc.org.cn/NewSite/NSMC/Home/Index.html; Wang et al. (2016)
Forest canopy height from Simard		1000 m × 1000 m; static.	Forest canopy height	https://webmap.ornl.gov/wcsdown/dataset.jsp?ds_id=10023; Simard et al. (2011)
Forest canopy height from Lang		0.5° × 0.5°; static.	Forest canopy height	https://doi.org/10.5281/zenodo.5704852; Lang et al. (2021)
SPAM V2.0		0.0833° × 0.0833°; static.	Cropland distribution map	https://doi.org/10.7910/DVN/PRFF8V; International Food Policy Research Institute (2019)
Cropland height		Static	Height for various cropland	Details in Table S3; Allen et al. (1998)
GRA and tundra height		Static	Typical height for the 5 CSCS-based GRA groups	Details in Table S2
CO_2 concentration		Monthly; 1958−present.	CO_2 concentration	https://gml.noaa.gov/ccgg/trends/data.html; Thoning et al. (2022)

Note: Due to unavailable minimum and maximum temperatures for the monthly ERA5 and MERRA-2 datasets, monthly values of the two variables were extracted from their hourly datasets.